ON THE EXISTENCE OF GENERALIZED BREATHERS AND TRANSITION FRONTS IN TIME-PERIODIC NONLINEAR LATTICES

CHRISTOPHER CHONG*, DMITRY E. PELINOVSKY†, AND GUIDO SCHNEIDER ‡

Abstract. We prove the existence of a class of time-localized and space-periodic breathers (called q-gap breathers) in nonlinear lattices with time-periodic coefficients. These q-gap breathers are the counterparts to the classical space-localized and time-periodic breathers found in space-periodic systems. Using normal form transformations, we establish rigorously the existence of such solutions with oscillating tails (in the time domain) that can be made arbitrarily small, but finite. Due to the presence of the oscillating tails, these solutions are coined generalized q-gap breathers. Using a multiple-scale analysis, we also derive a tractable amplitude equation that describes the dynamics of breathers in the limit of small amplitude. In the presence of damping, we demonstrate the existence of transition fronts that connect the trivial state to the time-periodic ones. The analytical results are corroborated by systematic numerical simulations.

1. Introduction. The classical discrete breather is a fundamental coherent structure of nonlinear lattices. They can be found in many fields, ranging from photonics, electrical circuits, condensed matter physics, molecular biology, chemistry, and phononics [12]. Breathers are relevant for applications, such as information storage and transfer in the context of photonic crystals [4], but are also rich mathematically and have inspired countless numerical and analytical studies [23, 9]. The discrete breather is localized in space and periodic in time with temporal frequency lying within a frequency gap [12]. Spatially periodic media can have frequency gaps, and hence, discrete breathers are possible in such systems [21].

If breathers can be found in the frequency gap of spatially periodic media, what can be found in the wavenumber gap of temporally periodic media? While this question is a natural one to ask, it has only been very recently addressed. In the context of a photonic time crystal, it was formally shown in [34] that structures that are localized in time and periodic in space can be found in the wavenumber bandgap of temporally periodic media. The structure reported on had same defining features as the classic breather, but with the role of space and time switched. Such solutions are called q-gap breathers, where q stands for the wavenumber.

In the presence of damping, so-called transition fronts are possible in a q-gap, which connect the trivial state to time-periodic ones. q-gap breathers and transition fronts were studied numerically and experimentally in the context of a nonlinear phononic lattice in [7]. The experimental platform therein was based on the one developed in [25], where bifurcations of time-periodic solutions were studied.

It is the purpose of this paper to establish rigorously the existence of q-gap breathers and transition fronts and to provide a tractable analytical approximation of their dynamics. q-gap breathers are a new type of structure, and are distinct from q-breathers, which are localized in wavenumber and periodic in time [13]. Temporal localization can also be achieved via other mechanisms, including zero-wavenumber gain modulation instability [29] and nonlinear resonances [5, 46]. Integrable equations admit such solutions explicitly, e.g., the Akhmediev breathers of the nonlinear Schrödinger (NLS) equation [1] and its discrete counterpart, the Ablowitz-Ladik lattice [2]. A feature that distinguishes q-gap breathers from other temporally localized structures, like the ones just described, is the fact that the underlying wavenumber lies in a q-gap.

*Department of Mathematics, Bowdoin College, Brunswick, ME 04011, USA
e-mail: cchong@bowdoin.edu.
†Department of Mathematics and Statistics, McMaster University, Hamilton, Ontario, Canada, L8S 4K1
e-mail: dmpeli@math.mcmaster.ca
‡Institut für Analysis, Dynamik und Modellierung, Universität Stuttgart, 70569 Stuttgart, Germany
e-mail: guido.schneider@mathematik.uni-stuttgart.de

Wavenumber bandgaps for the (possible) existence of q-gap breathers can be found in a wide class of temporally periodic lattices. Indeed, there have been many recent advances in experimental platforms for time-varying systems, including photonic [41, 44, 45, 32], electric [35, 27, 36], and phononic examples [38, 42, 31, 33, 24]. Controllable temporal localization has potential applications in the creation of phononic frequency combs [16] (see also [5, 46]), energy harvesting [28, 39], or acoustic signal processing [19]. The alternate mechanism for temporal localization that q-gap breathers afford and the wide availability of platforms in which they may be implemented suggest the potential utility of q-gap breathers in photonic, phononic, electrical, and even chemical or biological applications [7].

1.1. Model equations and physical motivation. The mathematical model for the present study is a time-periodic nonlinear lattice,

$$\underline{m}\ddot{u}_n + c\dot{u}_n + k(t)u_n = F(u_{n+1} - u_n) - F(u_n - u_{n-1}) \tag{1.1}$$

with mass $\underline{m}$, damping parameter $c \geq 0$, the time-periodic modulation of the spring parameter $k(t) = k(t+T)$ for a period $T > 0$, and the inter-particle force F. Assuming Dirichlet boundary conditions $u_0(t) = u_{N+1}(t) = 0$ for some integer N, we have a $2N$-dimensional dynamical system obtained from (1.1) at $n = 1, 2, \ldots, N$. We use $U := (u_1, u_2, \ldots, u_N)$ for further references in the main results.

We will consider a polynomial form of the inter-particle force

$$F(w) = K_2 w - K_3 w^2 + K_4 w^3, \qquad K_2 > 0 \tag{1.2}$$

in which Eq. (1.1) corresponds to the classical Fermi-Pasta-Ulam-Tsingou (FPUT) lattice if $k(t) = 0$ and $c = 0$ [11, 15]. The FPUT lattice is a central equation in the study of nonlinear waves [43], partly due to its relevance as a model in phononic, electrical, and biological systems (among others), its mathematical richness [3], and its place in history as the first test-bed for numerical simulations [8].

One concrete motivation for studying system (1.1) with a time-periodic stiffness term $k(t) = k(t+T)$ is that it describes an array of repelling magnets surrounded by time modulated coils. It was in this setting that q-gap breathers were observed experimentally [7]. In this case $F(w)$ models the repulsive force of the magnets, and is given by

$$F(w) = -\frac{a_1}{(d+w)^{a_2}}, \tag{1.3}$$

where $d, a_1, a_2 > 0$ are material parameters. Using the Taylor expansion of Eq. (1.3) at $w = 0$ gives a correspondence to the FPUT model with F given by Eq. (1.2) with

$$K_2 = \frac{a_2 a_1}{d^{a_2+1}}, \quad K_3 = \frac{a_2(a_2+1)a_1}{2d^{a_2+2}}, \quad K_4 = \frac{a_2(a_2+1)(a_2+2)a_1}{6d^{a_2+3}}. \tag{1.4}$$

For $k(t) = k(t+T)$, we will use a specific choice for illustrations that is motivated by the experimental set-up of [7]. In particular, we consider a piecewise constant time-periodic parameter function $k(t)$ in the form:

$$k(t) = \begin{cases} k_a, & t \in [0, \tau_d T), \\ k_b, & t \in [\tau_d T, T), \end{cases} \tag{1.5}$$

for a $\tau_d \in [0, 1]$ and where k_a, k_b are the so-called modulation amplitude parameters and τ_d is the duty-cycle. Using the rescaling

$$u_n(t) \to \frac{K_2}{K_3} u_n \left(\sqrt{\frac{K_2}{\underline{m}}} t \right)$$

leads to the normalized parameter values with $\underline{m}, K_2, K_3 \to 1$. We note that the results of this paper are applicable for more general parameter choices and time-periodic coefficients $k(t) = k(t+T)$ and to lattices with $K_j(t) = K_j(t+T)$ for $j = 2, 3, \ldots$.

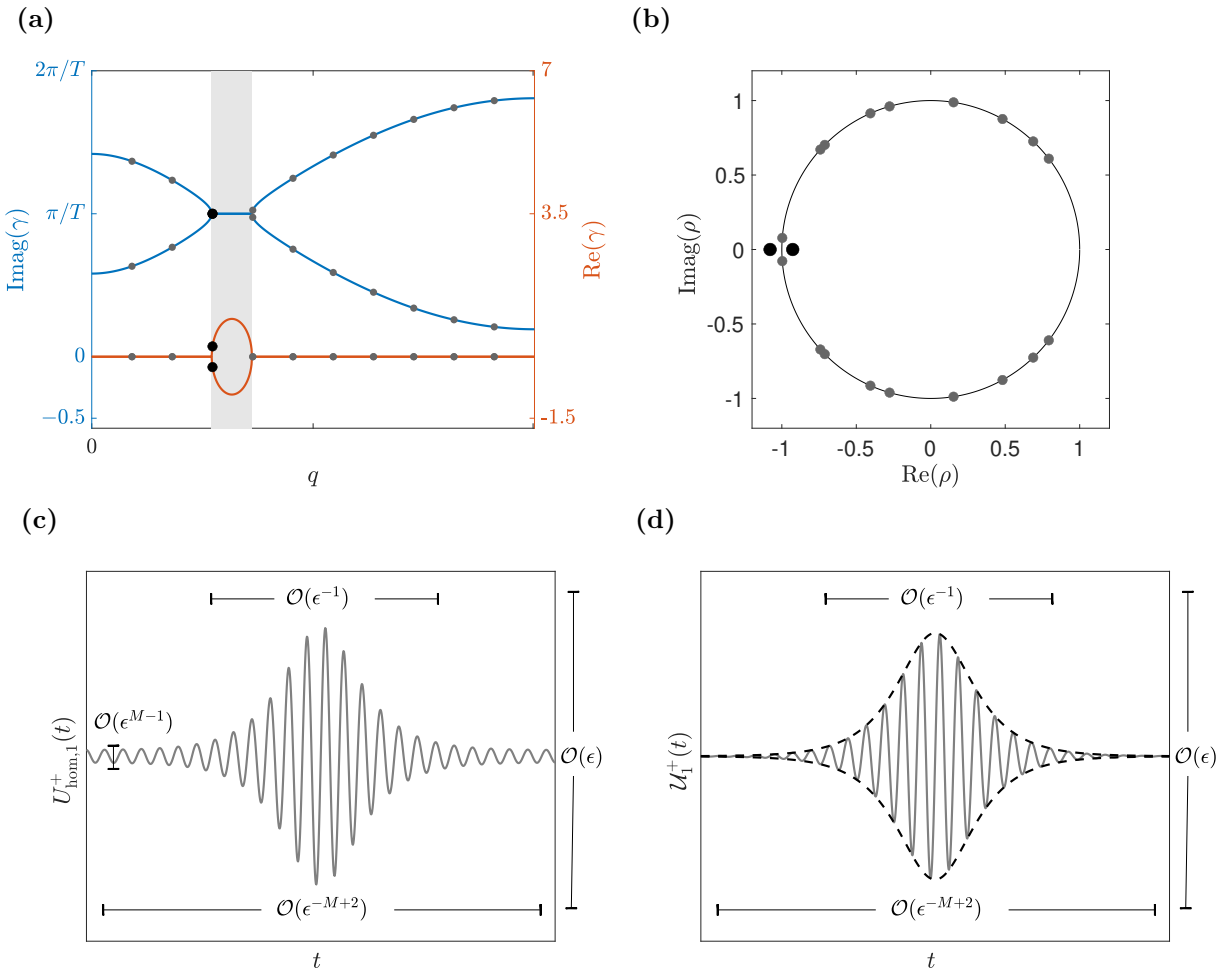

FIG. 1.1. ***(a)*** *The real (red) and imaginary (blue) part of the Floquet exponent γ as a function of Fourier wavenumber $q \in [0, \pi]$ in the infinite lattice. The gray shaded region corresponds to the wavenumber bandgap. The gray markers correspond to the Floquet exponents with a lattice size of $N = 10$. The $m_0 = 3$ exponents lie in wavenumber bandgap (larger black markers). The parameter values are $\underline{m} = K_2 = 1$, $c = 0$, $T = 1/0.37$, $\tau_d = 0.5$, $k_a = 0.6$ and $k_b = 0.8$.* ***(b)*** *Floquet multipliers corresponding to panel (a). One of the $m_0 = 3$ multipliers (larger black markers) has modulus exceeding unity.* ***(c)*** *Conceptualization of a generalized q-gap breather. The first component of $U^+_{\rm hom} = (u_1, u_2, \ldots, u_N)$ is shown.* ***(d)*** *The analytical approximation of the solution shown in panel (c), namely $\mathcal{U}^+$. The first component of $\mathcal{U}^+$ is shown.*

1.2. Summary of main results. We will develop rigorous proofs of the existence of oscillating homoclinic solutions for $c = 0$ and heteroclinic solutions for small damping $c > 0$ of Eq. (1.1) with time-periodic stiffness $k(t)$. Since the tails of homoclinic solutions have small oscillations that do not vanish at infinity, the solutions can also be thought of as generalized q-gap breathers. Similar nomenclature has been adopted of the description of classical breathers with non-zero tails in space-time continuous systems [17] and with spatially periodic coefficients [10]. See [14] for discussion of how the interchange of time and space variables affects derivation and justification of the homoclinic solutions.

Before stating the main theorems of the paper, let us describe intuitively the generalized q-gap breathers for $c = 0$. In the presence of time-periodic stiffness $k(t)$, some wavenumbers may fit into the gap in the dispersion relationship, as seen in Fig. 1.1(a). The corresponding Floquet multipliers are shown in panel (b)

(details on the Floquet theory follow in Sec. 2). Unlike the situation for frequency gaps in (linear) spatially periodic media, exponential growth of Fourier modes occurs if the wavenumber is inside the gap of the dispersion relation since the Floquet exponent in the gap has positive real part, or equivalently, the Floquet multiplier has modulus exceeding unity. Due to this (parametric) instability, initializing Eq. (1.1) with such a Fourier mode will initially lead to growth. However, as the amplitude increases, the nonlinearity of the system comes into play, and, as we shall prove later, has a localizing affect on the dynamics, see Fig. 1.1(c). This solution, however, cannot decay to zero. This is due to the presence of neutrally stable modes (i.e., the Floquet multipliers lying on the unit circle). During the dynamic evolution, all of the Fourier modes will couple (due to the nonlinearity). The presence of the neutrally stable modes causes the small oscillations, as seen in the tails of Fig. 1.1(c). From a dynamical systems point of view, the trivial state has one unstable direction, one stable direction, and $2N-2$ neutral directions. While genuine homoclinic solutions could be found in the intersection of the associated one-dimensional stable and unstable manifolds, it cannot be expected that such an intersection exists in an $2N$-dimensional phase space. Thus, only homoclinic solutions with small oscillating ripples for $|t| \to \infty$ exist. These solutions lie in the intersection of the $2N-1$-dimensional center-stable manifold with the $2N-1$-dimensional center-unstable manifold of the origin, for which we use the time-reversibility of the system (1.1) with $k(t)$ given by (1.5). The distance the wavenumber of the unstable Fourier mode is to the edge of the gap defines a small parameter $\varepsilon > 0$ (how exactly is detailed in Sec. 2). With normal form transformations for time-periodic systems (details in Secs. 3-6) it can be shown that the oscillating ripples can be made arbitrarily small, i.e., of order $\mathcal{O}(\varepsilon^{M-1})$ at the time scale of $\mathcal{O}(\varepsilon^{-M+2})$ with some $M \in \mathbb{N}$ arbitrarily large but fixed, see Fig. 1.1(c). Using a multiple-scale analysis (details in Sec. 7), one can derive an explicit approximation of a genuine homoclinic orbit, see Fig. 1.1(d), which agrees with the leading order of the generalized breather's profile.

We are now ready to present the main theorem on the existence of two homoclinic orbits with oscillating ripples, i.e., generalized q-gap breathers. The assumptions **(Spec)** and **(Coeff)** are described in Secs. 2 and 5 respectively. The small parameter ε is defined in **(Spec)** and explicitly in the representation for $k(t) = k(t+T)$.

THEOREM 1.1. *Assume the spectral condition* **(Spec)** *and the normal form coefficient condition* **(Coeff)** *are satisfied. Then for every $M \in \mathbb{N}$ with $M \geq 3$ there exists an $\varepsilon_0 > 0$ and $C_0 > 0$ such that for all $\varepsilon \in (0, \varepsilon_0)$ the system (1.1) with the time-periodic coefficient (1.5) and $c = 0$ possesses two generalized homoclinic solutions $U^{\pm}_{\rm hom} \in C^1([-\varepsilon^{-M+2}, \varepsilon^{-M+2}], \mathbb{R}^N)$ satisfying*

$$\sup_{t \in [-\varepsilon^{-M+2}, \varepsilon^{-M+2}]} \|U^{\pm}_{\rm hom}(t) - \mathcal{U}^{\pm}(t)\| + \|(U^{\pm}_{\rm hom})'(t) - (\mathcal{U}^{\pm})'(t)\| \leq C_0 \varepsilon^{M-1}$$

where $\mathcal{U}^{\pm}(t) : \mathbb{R} \to \mathbb{R}^N$ satisfy $\lim_{|t| \to \infty} \|\mathcal{U}^{\pm}(t)\| + \|(\mathcal{U}^{\pm})'(t)\| = 0$ and can be approximated as

$$(\mathcal{U}^{\pm})_n(t) = \pm \varepsilon A(\varepsilon t) g(t) \sin(q_{m_0} n) + \mathcal{O}(\varepsilon^2),$$

where $g(t+T) = -g(t)$ and $A(\tau) = \alpha \operatorname{sech}(\beta \tau)$ are uniquely defined, real-valued functions with some $\alpha, \beta > 0$, see Eq. (8.1) below.

In case of small damping $c = \mathcal{O}(\varepsilon)$ each of the two homoclinic orbits $U^{\pm}_{\rm hom}$ of Theorem 1.1 breaks up. There exist two non-zero anti-periodic solutions $\mathcal{U}^{\pm}_{\rm per}(t+T) = -\mathcal{U}^{\pm}_{\rm per}(t)$ with a $2N$-dimensional stable manifold for $c > 0$.

Therefore, as can be seen by counting the dimensions, the one-dimensional unstable manifold from the zero equilibrium intersects the $2N$-dimensional stable manifolds of one the two non-zero anti-periodic solutions $\mathcal{U}^{\pm}_{\rm per}$ transversally. In contrast to the oscillating homoclinic orbits, the heteroclinic orbits have no oscillating ripples as $t \to -\infty$ and converge to the orbits of the anti-periodic solutions $\mathcal{U}^{\pm}_{\rm per}$ as $t \to +\infty$, see Figure 1.2.

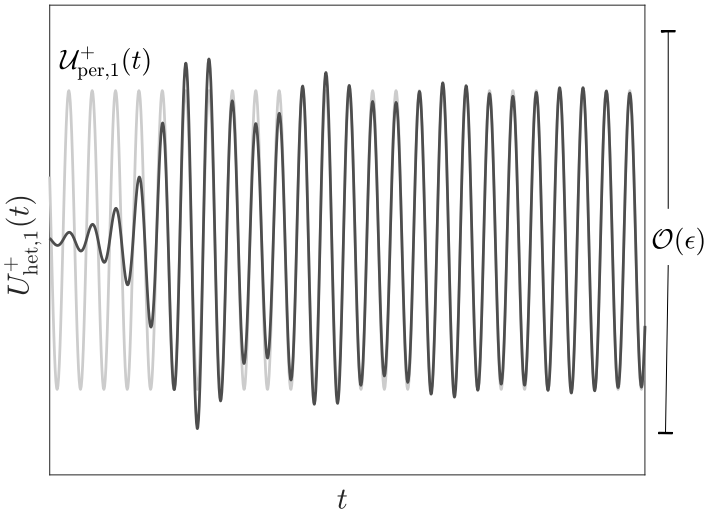

FIG. 1.2. *Example of the transition front* $U^+_{\mathrm{het}} = (u_1, u_2, \dots, u_N)$*, where the first component is shown. The first component of the anti-periodic solution* $\mathcal{U}^+_{\mathrm{per}}$ *is also shown as the light gray line.*

Existence of the anti-periodic solutions $\mathcal{U}^{\pm}_{\mathrm{per}}$ is guaranteed by the following theorem.

THEOREM 1.2. *Assume the spectral condition* **(Spec)** *and the normal form coefficient condition* **(Coeff)**. *Fix* $\widetilde{c} \geq 0$. *Then there exists an* $\varepsilon_0 > 0$ *and* $C_0 > 0$ *such that for all* $\varepsilon \in (0, \varepsilon_0)$ *the system* (1.1) *with the time-periodic coefficient* (1.5) *and* $c = \widetilde{c}\varepsilon > 0$ *possesses anti-periodic solutions* $\mathcal{U}^{\pm}_{\mathrm{per}}$ *such that* $\mathcal{U}^{\pm}_{\mathrm{per}}(t+T) = -\mathcal{U}_{\mathrm{per}}(t)$ *and*

$$\sup_{t\in\mathbb{R}} \|\mathcal{U}^{\pm}_{\mathrm{per}}(t)\| + \|(\mathcal{U}^{\pm}_{\mathrm{per}})'(t)\| \leq C_0\varepsilon.$$

The following theorem presents the main result on the existence of the heteroclinic orbits (transition fronts) between the trivial solution 0 and the anti-periodic solutions $\mathcal{U}^{\pm}_{\mathrm{per}}$.

THEOREM 1.3. *Assume the spectral condition* **(Spec)** *and the normal form coefficient condition* **(Coeff)**. *Fix* $\widetilde{c} > 0$. *Then there exists an* $\varepsilon_0 > 0$ *such that for all* $\varepsilon \in (0, \varepsilon_0)$ *the system* (1.1) *with the time-periodic coefficient* (1.5) *and* $c = \widetilde{c}\varepsilon > 0$ *possesses two heteroclinic solutions* $U^{\pm}_{\mathrm{het}} \in C^1(\mathbb{R}, \mathbb{R}^N)$ *such that*

$$\lim_{t\to-\infty} U^{\pm}_{\mathrm{het}}(t) = 0, \qquad \lim_{t\to-\infty} (U^{\pm}_{\mathrm{het}})'(t) = 0$$

and

$$\lim_{t\to+\infty} \inf_{t_0\in[0,T]} \|U^{\pm}_{\mathrm{het}}(t) - \mathcal{U}^{\pm}_{\mathrm{per}}(t+t_0)\| + \|(U^{\pm}_{\mathrm{het}})'(t) - (\mathcal{U}^{\pm}_{\mathrm{per}})'(t+t_0)\| = 0,$$

where $\mathcal{U}^{\pm}_{\mathrm{per}}$ *are the anti-periodic solutions of* (1.1) *from Theorem 1.2.*

Remark 1.4. Because of the quadratic nonlinearity in the FPUT system (1.1), the homoclinic, anti-periodic, and heteroclinic orbits in Theorems 1.1-1.3 are not related by the sign reflection even though the leading orders obtained from the cubic normal form are related by the sign reflection, see Eq. (7.18). However, if $K_3 = 0$, these orbits are related by the sign reflection up to any orders due to the symmetry of the FPUT system (1.1).

The article is organized as follows. Section 2 presents the Floquet and spectral analysis of the linearized FPUT system and introduce assumption (**Spec**). Preparations for the normal form transformations are

described in Section 3. Normal form transformations are described in Section 4. The proof of Theorem 1.1 is given in Section 5, where assumption (**Coeff**) is introduced. Section 6 contains the proof of Theorems 1.2 and 1.3. A multiple-scale analysis is carried out in Section 7, which provides tractable approximations for both breathers and fronts. It also allows verification of (**Coeff**) through direct computation. Numerical illustrations of the main results are described in Section 8. Section 9 concludes the paper with a summary and brief discussions.

Funding: This work was partially supported by the National Science Foundation under grant number DMS-2107945 (C. Chong). D. E. Pelinovsky is partially supported by AvHumboldt Foundation as Humboldt Research Award. G. Schneider is partially supported by the Deutsche Forschungsgemeinschaft DFG through the cluster of excellence 'SimTech' under EXC 2075-390740016.

2. The linearized system. The linearized FPUT system at the trivial (zero) equilibrium is given by

$$\underline{m}\ddot{u}_n + c\dot{u}_n + k(t)u_n = K_2(u_{n+1} - 2u_n + u_{n-1}) \tag{2.1}$$

for $n = 1, 2, \ldots, N$ with Dirichlet boundary conditions $u_0(t) = u_{N+1}(t) = 0$. The linearized system (2.1) is solved by a linear superposition of the discrete Fourier sine modes:

$$u_n(t) = \sum_{m=1}^{N} \widehat{u}_m(t) \sin(q_m n), \quad q_m := \frac{\pi m}{N+1}, \quad 1 \leq m \leq N.$$

The m-th Fourier mode has the amplitude $\widehat{u}_m(t)$ for which the linear FPUT equation (2.1) transforms to the linear Schrödinger equation

$$\mathcal{L}\widehat{u}_m = K_2\omega^2(q_m)\widehat{u}_m, \tag{2.2}$$

where

$$\mathcal{L} := -\underline{m}\partial_t^2 - c\partial_t - k(t), \quad k(t+T) = k(t)$$

and

$$\omega^2(q) := 4\sin^2\left(\frac{q}{2}\right), \quad q \in [0, \pi].$$

We will review solutions of the spectral problem (2.2) by using the Floquet theory and the spectral theory of the Schrödinger operators.

2.1. Floquet theory. To obtain the monodromy matrix associated to (2.2) for general time-periodic coefficients $k(t)$, one may resort to numerical computation or perturbation analysis [26]. However, in the case of piecewise constant $k(t)$ as in (1.5), this can be done explicitly [6, 37] (see also [7]). For the convenience of the readers, we summarize the relevant results.

Let $\lambda_m := K_2\omega^2(q_m)$ for each $1 \leq m \leq N$, and define $s_a, s_b > 0$ by

$$s_{a,b} := \sqrt{\frac{\lambda_m + k_{a,b}}{\underline{m}} - \frac{c^2}{4\underline{m}^2}}. \tag{2.3}$$

Note that s_a, s_b also depend on $m = 1, 2, \ldots, N$ but the index m is dropped from the notation for simplicity. We obtain the exact solution of (2.2):

$$\widehat{u}_m(t) = \begin{cases} e^{-\frac{ct}{2\underline{m}}}\left[A_0\cos(s_a t) + B_0\sin(s_a t)\right], & t \in [0, \tau_d T), \\ e^{-\frac{ct}{2\underline{m}}}\left[C_0\cos(s_b(t-\tau_d T)) + D_0\sin(s_b(t-\tau_d T))\right], & t \in [\tau_d T, T), \end{cases} \tag{2.4}$$

with some constants A_0, B_0, C_0, D_0. By C^1-continuity across $t = \tau_d T$, we obtain

$$\begin{bmatrix} C_0 \\ D_0 \end{bmatrix} = \begin{bmatrix} \cos(s_a\tau_d T) & \sin(s_a\tau_d T) \\ -\frac{s_a}{s_b}\sin(s_a\tau_d T) & \frac{s_a}{s_b}\cos(s_a\tau_d T) \end{bmatrix} \begin{bmatrix} A_0 \\ B_0 \end{bmatrix}. \tag{2.5}$$

The monodromy matrix J is obtained as a mapping

$$\begin{cases} \widehat{u}_m(0) = A_0, \\ \widehat{u}_m'(0) = s_a B_0 - \frac{c}{2\underline{m}} A_0 \end{cases} \quad \Rightarrow \quad \begin{cases} \widehat{u}_m(T) = e^{-\frac{cT}{2\underline{m}}} A_1, \\ \widehat{u}_m'(T) = e^{-\frac{cT}{2\underline{m}}} \left[s_a B_1 - \frac{c}{2\underline{m}} A_1 \right], \end{cases} \tag{2.6}$$

with

$$\begin{bmatrix} A_1 \\ B_1 \end{bmatrix} = \begin{bmatrix} \cos(s_b(1-\tau_d)T) & \sin(s_b(1-\tau_d)T) \\ -\frac{s_b}{s_a}\sin(s_b(1-\tau_d)T) & \frac{s_b}{s_a}\cos(s_b(1-\tau_d)T) \end{bmatrix} \begin{bmatrix} C_0 \\ D_0 \end{bmatrix} =: J \begin{bmatrix} A_0 \\ B_0 \end{bmatrix}. \tag{2.7}$$

Since $\det(J) = 1$ and

$$\operatorname{trace}(J) = 2\cos(s_a\tau_d T)\cos(s_b(1-\tau_d)T) - \frac{s_a^2 + s_b^2}{s_a s_b}\sin(s_a\tau_d T)\sin(s_b(1-\tau_d)T), \tag{2.8}$$

the eigenvalues ρ_1 and ρ_2 of J satisfies

$$\rho_1\rho_2 = 1, \quad \rho_1 + \rho_2 = \operatorname{trace}(J),$$

with only three possibilities:

- $\operatorname{trace}(J) > 2$ implies $0 < \rho_1 < 1 < \rho_2 = \rho_1^{-1}$,
- $-2 \le \operatorname{trace}(J) \le 2$ implies $\rho_1 = \overline{\rho}_2 \in \mathbb{C}$ with $|\rho_{1,2}| = 1$,
- $\operatorname{trace}(J) < -2$ implies $\rho_2 = \rho_1^{-1} < -1 < \rho_1 < 0$.

The Floquet exponents of the mapping (2.6) are given by $\gamma_{1,2} = \upsilon_{1,2} - \frac{c}{2\underline{m}}$, where

- $\operatorname{trace}(J) > 2$ implies $\upsilon_{1,2} = \pm\log(\rho_2)/T$,
- $-2 \le \operatorname{trace}(J) \le 2$ implies $\upsilon_{1,2} = \pm i\arg(\rho_1)/T$,
- $\operatorname{trace}(J) < -2$ implies $\upsilon_{1,2} = i\pi/T \pm \log(|\rho_2|)/T$.

If $c = 0$, the trivial solution $U = 0$ is spectrally stable if all Floquet exponents are purely imaginary. This corresponds to the case with $-2 \le \operatorname{trace}(J) \le 2$. Figure 2.1(a) shows the Floquet multipliers ρ in the critical case where $\operatorname{trace}(J) = -2$ with $m = 3$. The corresponding Floquet exponents $\gamma = \upsilon$ are shown in Fig. 2.1(b).

2.2. Spectral theory. Let us review the spectral properties of the Schrödinger operator

$$\mathcal{L} : H^2(\mathbb{R}) \subset L^2(\mathbb{R}) \to L^2(\mathbb{R})$$

with a T-periodic coefficient $k(t) = k(t+T)$ in the particular case of $c = 0$. The spectrum of $\mathcal{L}$ is purely continuous and consists of bands disjoint from each other by some gaps:

$$\sigma(\mathcal{L}) = [\nu_0, \mu_1] \cup [\mu_2, \nu_1] \cup [\nu_2, \mu_3] \cup [\mu_4, \nu_3] \cup \cdots \tag{2.9}$$

where $\{\nu_j\}_{j=0}^{\infty}$ are eigenvalues of $\mathcal{L}f = \nu f$ with periodic boundary conditions $f(t+T) = f(t)$ and $\{\mu_j\}_{j=1}^{\infty}$ are eigenvalues of $\mathcal{L}g = \mu g$ with anti-periodic boundary conditions $g(t+T) = -g(t)$. Eigenvalues $\{\nu_j\}_{j=0}^{\infty}$ correspond to $\operatorname{trace}(J) = 2$ of the Floquet theory, whereas eigenvalues $\{\mu_j\}_{j=0}^{\infty}$ correspond to $\operatorname{trace}(J) = -2$ and the spectral bands correspond to $-2 \le \operatorname{trace}(J) \le 2$.

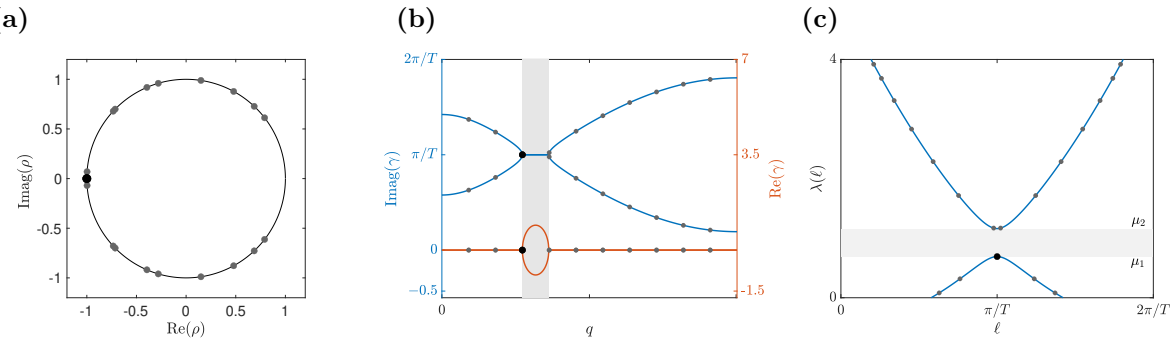

FIG. 2.1. *Bifurcation scenario for the parameter set* $\underline{m} = K_2 = 1$, $c = 0$, $T = 1/0.37$ *and* $\tau_d = 0.5$. *With the critical modulation amplitude parameters* $k_a^0 = 0.5$ *and* $k_b^0 = 0.79$, *the critical Fourier mode is* $m_0 = 3$. ***(a)*** *Plot of the Floquet multipliers,* ρ, *in the complex plane (the unit circle is shown for visual aid). The* $m_0 = 3$ *multiplier lies exactly at -1 on the unit circle (larger black marker).* ***(b)*** *The real (red) and imaginary (blue) part of the Floquet exponent* γ *as a function of Fourier wavenumber* $q \in [0, \pi]$ *in the infinite lattice. The gray shaded region corresponds to the wavenumber bandgap. The gray markers correspond to the Floquet exponents with a lattice size of* $N = 10$. *The* $m_0 = 3$ *exponent lies exactly at the left edge of the wavenumber bandgap (larger black marker).* ***(c)*** *Spectral bands (blue curves) of the Schrödinger operator as a function of* $\ell = \text{imag}(\gamma)$, *the imaginary part of the Floquet exponent. The gray dots show the corresponding values in the finite lattice with* $N = 10$. *The eigenvalues* μ_1 *and* μ_2 *define the edges of the band gap, shown as the gray shaded region. The* $m_0 = 3$ *mode lies exactly at the top of the first spectral band (larger black marker).*

Remark 2.1. Note that λ is parameterized by the wavenumber q in $\lambda = K_2\omega^2(q)$, which in turn determines the Floquet exponent γ. Within the spectral bands, the corresponding Floquet exponents are purely imaginary and are of the form $\gamma = i\ell$. An example plot showing the dependence of λ on ℓ is shown in Fig. 2.1(c). For this example there is one band gap, which is the shaded region in the figure. The band gap edges are given by μ_1 (the bottom of the gap) and μ_2 (the top of the gap). This representation of the spectrum will be useful later when we derive an amplitude equation for the description of the envelope of the breather in Sec. 7. In particular, the concavity of $\lambda(\ell)$ will play a key role.

We define *the bifurcation* for a particular stiffness $k(t) \equiv k_0(t)$, for which $\mathcal{L} \equiv \mathcal{L}_0$, if there exists an integer $1 \leq m_0 \leq N$ such that $\lambda_{m_0} = K_2\omega^2(q_{m_0})$ coincides with the end point of $\sigma(\mathcal{L}_0)$ and $\lambda_m = K_2\omega^2(q_m)$ for $m \neq m_0$ are located inside $\sigma(\mathcal{L}_0)$. For the bifurcation shown in Figure 2.1, λ_{m_0} coincides with μ_1, for which the two bifurcating Floquet exponents are given by $\gamma_0 = i\frac{\pi}{T}$ with $\ell_0 := \frac{\pi}{T}$. This bifurcation corresponds to $\lambda_1''(\ell_0) < 0$ and

$$[0, 4K] \subset [\nu_0, \nu_1], \quad K_2\omega^2(q_{m_0}) = \mu_1. \tag{2.10}$$

Equivalently, we can obtain a bifurcation when λ_{m_0} coincides with μ_2 with $\lambda_2''(\ell_0) > 0$ and

$$[0, 4K] \subset [\nu_0, \nu_1], \quad K_2\omega^2(q_{m_0}) = \mu_2. \tag{2.11}$$

The two bifurcating Floquet exponents γ_0 correspond to the Floquet multiplier ρ at -1. All other Floquet exponents γ are assumed to be on the imaginary axis bounded away from 0 and γ_0. The corresponding Floquet multipliers ρ are on the unit circle bounded away from $+1$ and -1.

The bifurcation in terms of Floquet multipliers is shown in Fig. 2.1(a), whereas Fig. 2.1(b) shows the bifurcation in terms of Floquet exponents. The spectral bands of the Schrödinger operator $\mathcal{L}_0$ are shown in Fig. 2.1(c). Notice that the discrete mode $m_0 = 3$ lies exactly at $(\ell, \lambda) = (\ell_0, \mu_1)$, where $\ell_0 = \frac{\pi}{T}$.

2.3. Spectral assumption and defining the small parameter ε. With the linear theory in hand, we can now specify the spectral assumption as follows.

(Spec) *There exists a periodic coefficient $k_0(t+T) = k_0(t)$, for which all Floquet exponents lie on the imaginary axis. With the exception of two exponents at $\frac{i\pi}{T}$, they are assumed to be simple and non-zero. For small $\varepsilon > 0$ we assume that the two Floquet exponents at $\frac{i\pi}{T}$ split symmetrically from the imaginary axis along the real axis to the order of $\mathcal{O}(\varepsilon)$.*

We can define ε more explicitly by using the decomposition

$$k(t) = k_0(t) + \delta\varepsilon^2, \tag{2.12}$$

where δ is a proper sign factor. For $c = 0$, the small parameter ε is related to the distance of the critical Floquet exponents $\gamma = \upsilon$ from the imaginary axis in the following way. The real part of the Floquet exponent γ which depends on ε is given by

$$\mathrm{Re}(\gamma) = \frac{1}{T}\cosh^{-1}\left(-\frac{1}{2}\mathrm{trace}(J)\right).$$

Since we know from (**Spec**) that $\mathrm{trace}(J) = -2$ with $\varepsilon = 0$ (for $k(t) = k_0(t)$), a series expansion of the real part of the Floquet exponent about $\varepsilon = 0$ yields $\mathrm{Re}(\gamma) = \mathcal{O}(\varepsilon)$, where we used the fact that $\cosh^{-1}(1+w) \approx \sqrt{2w}$ and $\mathrm{trace}(J) = -2 + \mathcal{O}(\varepsilon^2)$. In Sec. 7.2 we will show that

$$\mathrm{Re}(\gamma) = \varepsilon\frac{\sqrt{2}}{\sqrt{|\lambda''(\ell_0)|}} + \mathcal{O}(\varepsilon^2), \tag{2.13}$$

where $\lambda(\ell)$ is the corresponding band of $\mathcal{L}_0$ at $\ell_0 = \frac{\pi}{T}$ and the sign of δ is selected to be the opposite of the sign of $\lambda''(\ell_0)$.

Remark 2.2. One can relate the small parameter ε to the distance of the bifurcating wavenumber q_{m_0} to the band edge in the following way. For a fixed ε, suppose the wavenumber bandgap is $[q_\ell, q_r]$, where the left edge q_ℓ and right edge q_r depend on ε and can be found by solving $\mathrm{trace}(J) = -2$ with $\lambda = K_2\omega^2(q)$. Suppose that the critical wavenumber q_{m_0} coincides with the left band edge at the bifurcation point, (i.e., $q_{m_0} = q_\ell$ when $\varepsilon = 0$). Then, for $\varepsilon > 0$, the distance to the band edge is $\Delta q = q_\ell - q_{m_0}$. By inspection of (2.3) and (2.8), if one knows the critical values of k_a^0 and k_b^0 then Δq can be determined by solving $\lambda(\ell(q_{m_0})) = \lambda(\ell(q_{m_0} + \Delta q)) + \delta\varepsilon^2$ which yields

$$\Delta q = q_{m_0} - 2\sin^{-1}\left(\sqrt{\sin^2(q_{m_0}/2) - \frac{\delta\varepsilon^2}{4K_2}}\right) = \frac{\delta\varepsilon^2}{\partial_q\lambda(\ell(q_{m_0}))} + \mathcal{O}(\varepsilon^4). \tag{2.14}$$

Thus $\Delta q = \mathcal{O}(\varepsilon^2)$.

3. Normal form transformations. The FPUT system (1.1) consists of N oscillators with Dirichlet boundary conditions. By augmenting the vector $U(t) \in \mathbb{R}^N$ with $U'(t) \in \mathbb{R}^N$ as the vector $V(t) \in \mathbb{R}^{2N}$, we rewrite the $2N$-dimensional time-periodic system in the abstract form:

$$\dot{V}(t) = Q(t)V(t) + N(V(t)), \tag{3.1}$$

with the time-periodic coefficient matrix $Q(t) = Q(t+T) \in \mathbb{R}^{2N\times 2N}$ being piecewise continuous on $[0, T]$ for a period $T > 0$ and the nonlinear function $N(V) : \mathbb{R}^{2N} \to \mathbb{R}^{2N}$ being smooth at $V = 0$ with $N(0) = 0$ and $D_V N(0) = 0$. The solutions of the linear system

$$\dot{V}(t) = Q(t)V(t) \tag{3.2}$$

are, according to Floquet's theorem, of the form

$$V(t) = P(t)e^{\Lambda t}V(0) \tag{3.3}$$

with a T-time-periodic matrix function $P(t) = P(t+T) \in \mathbb{R}^{2N\times 2N}$ and a time-independent matrix $\Lambda \in \mathbb{R}^{2N\times 2N}$, eigenvalues of which coincide with Floquet exponents in Section 2.

Remark 3.1. Eigenvalues γ of the matrix Λ are uniquely defined in the strip:

$$-\frac{\pi}{T} < \text{Imag}(\gamma) \leq \frac{\pi}{T}. \tag{3.4}$$

Eigenvalues of Λ are generally complex-valued but we use the presentation (3.3) with real $P(t)$ and real Λ for convenience of the normal form transformations. For example, if $\gamma = \alpha \pm i\beta$ are two complex-conjugate eigenvalues of Λ, then the canonical form for the corresponding block of $\Lambda \in \mathbb{R}^{2N\times 2N}$ is

$$\left[\begin{array}{cc} \alpha & \beta \\ -\beta & \alpha \end{array}\right].$$

Remark 3.2. As preparations for the normal form transformation, we can consider the time-periodic system (3.1) on the double period $2T$. The advantage of this approach is that the bifurcating Floquet exponents in the stripe (3.4) correspond to zero Floquet exponents in the $2T$-periodic system. The solution (3.3) of the linear system (3.2) can be rewritten in the form:

$$V(t) = \widetilde{P}(t)e^{\widetilde{\Lambda}t}V(0), \tag{3.5}$$

with the time-periodic matrix function $\widetilde{P}(t) = \widetilde{P}(t+2T) \in \mathbb{R}^{2N\times 2N}$ and the time-independent matrix $\widetilde{\Lambda} \in \mathbb{R}^{2N\times 2N}$. According to the assumption (**Spec**) at the bifurcation point, $\widetilde{\Lambda}$ has a double zero eigenvalue and all other (purely imaginary) eigenvalues of $\widetilde{\Lambda}$ are simple and bounded away from 0.

Remark 3.3. For the normal form transformation in Section 4 we need the following property of $\widetilde{P}(t)$. Comparing the two representations of the fundamental matrix solution

$$\Phi(t) = P(t)e^{\Lambda t} = \widetilde{P}(t)e^{\widetilde{\Lambda}t},$$

we obtain

$$\widetilde{P}(t) = P(t)e^{\pi i t/T} = \sum_{m\in\mathbb{Z}} P_m e^{2\pi i m t/T} e^{\pi i t/T},$$

with P_m being constant $2N \times 2N$-matrices.

We now transform the system (3.1) on the double period to a convenient form for which the linear part is autonomous in t. Let $V(t) = \widetilde{P}(t)W(t)$, then $W(t) \in \mathbb{R}^{2N}$ satisfies the time-periodic system:

$$\dot{W}(t) = \widetilde{\Lambda}W(t) + \widetilde{P}(t)^{-1}N(\widetilde{P}(t)W(t)). \tag{3.6}$$

We define the projection Π_0 on the subspace associated with the double zero eigenvalue of $\widetilde{\Lambda}$ by

$$\Pi_0 = \frac{1}{2\pi i}\int_{\Gamma_0} (\lambda I - \widetilde{\Lambda})^{-1} d\lambda, \tag{3.7}$$

where Γ_0 is a closed curve surrounding the origin in the λ plane counter-clockwise. The projection on the two other $(2N-2)$ eigenvalues of $\widetilde{\Lambda}$ on the imaginary axis is defined by $\Pi_h = I - \Pi_0$. The range of Π_0 is two-dimensional and the range of Π_h is $(2N-2)$-dimensional.

We apply these projections on system (3.6) and find for $W_0 = \Pi_0 W$ and $W_h = \Pi_h W$ that

$$\dot{W}_0(t) = \Lambda_0 W_0(t) + N_0(W_0, W_h), \tag{3.8}$$

$$\dot{W}_h(t) = \Lambda_h W_h(t) + N_h(W_0, W_h) + H(W_0), \tag{3.9}$$

where we have introduced $\Pi_0\widetilde{\Lambda} = \Lambda_0\Pi_0$, $\Pi_h\widetilde{\Lambda} = \Lambda_h\Pi_h$,

$$N_0(W_0, W_h) := \Pi_0\widetilde{P}(t)^{-1}N(\widetilde{P}(t)W(t)),$$

$$N_h(W_0, W_h) + H(W_0) := \Pi_h\widetilde{P}(t)^{-1}N(\widetilde{P}(t)W(t)).$$

The splitting into $N_h(W_0, W_h) + H(W_0)$ is justified with $N_h(W_0, 0) = 0$. System (3.8)-(3.9) is extended by the additional equation $\dot{\varepsilon} = 0$, where ε is the bifurcation parameter in (**Spec**).

Remark 3.4. In the context of the time-periodic system (3.6) on the double period, we recall that W_0 represents the modes associated to the two Floquet exponents which split from the double zero and leave the imaginary axis and that W_h represents the modes associated to the other $(2N-2)$ Floquet exponents which stay on the imaginary axis for small bifurcation parameter ε.

We use the normal form transformations to reduce the order of $H(W_0)$ in terms of powers of $\|W_0\|$.

LEMMA 3.5. *For every $M \geq 2$ there exists an $\varepsilon_0 > 0$ such that for all $\varepsilon \in (0, \varepsilon_0)$ there exists a change of coordinates*

$$W_{0,M} = W_0, \qquad W_{h,M} = W_h + G(W_0)$$

such that system (3.8)-(3.9) transforms into

$$\dot{W}_0 = \Lambda_0 W_0 + N_{0,M}(W_0, W_{h,M}), \tag{3.10}$$

$$\dot{W}_{h,M} = \Lambda_h W_{h,M} + N_{h,M}(W_0, W_{h,M}) + H_M(W_0), \tag{3.11}$$

with $N_{h,M}(W_0, 0) = 0$ and $H_M(W_0) = \mathcal{O}(\|W_0\|^M)$.

Proof. We set $W_{h,2} = W_h$ and then inductively

$$W_{h,n+1} = W_{h,n} + G_n(W_0),$$

with $G_n(W_0)$ being a n-linear mapping in W_0. After the transformations we have a system of the form

$$\dot{W}_0 = \Lambda_0 W_0 + N_{0,n+1}(W_0, W_{h,n+1}), \tag{3.12}$$

$$\dot{W}_{h,n+1} = \Lambda_h W_{h,n+1} + N_{h,n+1}(W_0, W_{h,n+1}) + H_{n+1}(W_0), \tag{3.13}$$

with

$$\begin{aligned}
N_{0,n+1}(W_0, W_{h,n+1}) &= N_{0,n}(W_0, W_{h,n} - G_n(W_0)), \\
N_{h,n+1}(W_0, W_{h,n+1}) &= N_{h,n}(W_0, W_{h,n} - G_n(W_0)) \\
&\quad -(D_{W_0} G_n(W_0))(N_{0,n}(W_0, W_{h,n}) - N_{0,n}(W_0, 0)), \\
H_{n+1}(W_0) &= H_n(W_0) + \Lambda_h G_n(W_0) \\
&\quad -(D_{W_0} G_n(W_0))(\Lambda_0 W_0 + N_{0,n}(W_0, 0)),
\end{aligned}$$

and so $N_{h,n+1}(W_0, 0) = 0$. In order to have $H_{n+1}(W_0) = \mathcal{O}(\|W_0\|^{n+1})$ if $H_n(W_0) = \mathcal{O}(\|W_0\|^n)$ we have to choose G_n such that

$$H_{n,n}(W_0) + \Lambda_h G_n(W_0) - (D_{W_0} G_n(W_0))\Lambda_0 W_0 = 0, \tag{3.14}$$

where $H_{n,n}(W_0)$ is the n-linear part of $H_n(W_0)$, i.e. $H_n(W_0) - H_{n,n}(W_0) = \mathcal{O}(\|W_0\|^{n+1})$. Since

$$H_{n,n}(W_0)(t) = H_{n,n}(W_0)(t + 2T)$$

we also have to choose $G_n(W_0)(t) = G_n(W_0)(t + 2T)$. Using Fourier series

$$G_n(W_0)(t) = \sum_{m \in \mathbb{Z}} G_n(W_0)[m] e^{\pi i m t / T}$$

it is easy to see that (3.14) can be solved w.r.t. G_n since according to the assumption (**Spec**), none of the eigenvalues λ_j of Λ_h are located at 0 and Λ_0 has a double zero eigenvalue. As a result, the term $H(W_0)$ can be made arbitrarily small in terms of powers of $\|W_0\|$. ∎

Remark 3.6. The sequence of normal form transformations is not convergent and so we stop after $M-1$ transformations with some large but fixed $M \in \mathbb{N}$, for which we have $H_M(W_0) = \mathcal{O}(\|W_0\|^M)$. Note that the minimum of $H_M(W_0)$ is attained for $M = \mathcal{O}(1/\|W_0\|)$-many transformations, after which H_M is exponentially small in terms of $\|W_0\|$, cf. [30].

4. Normal form transformations for the reduced system. If we ignore the terms $H_M(W_0)$ in (3.10)-(3.11), then $\{W_{h,M} = 0\}$ is an invariant subspace for (3.10)-(3.11). In this two-dimensional subspace the reduced system is obtained by setting $W_{h,M} = 0$ in the first equation. So we consider the two-dimensional ODE

$$\dot{W}_0 = \Lambda_0 W_0 + N_{0,M}(W_0, 0). \tag{4.1}$$

At the bifurcation point Λ_0 posseses a double eigenvalue $\lambda = 0$ with algebraic multiplicity two and geometric multiplicity one. Thus, we have a Jordan-block of size two. The eigenvector of $\widetilde{\Lambda}$ is denoted with φ_1 and the generalized eigenvector with φ_2, i.e. $\widetilde{\Lambda}\varphi_1 = 0$ and $\widetilde{\Lambda}\varphi_2 = \varphi_1$. If we introduce coordinates A, B by

$$W_0 = A\varphi_1 + B\varphi_2 \tag{4.2}$$

we can rewrite (4.1) as the following two-dimensional system

$$\dot{A} = B + f_A(t, A, B), \tag{4.3a}$$
$$\dot{B} = \widetilde{\varepsilon}^2 A + f_B(t, A, B), \tag{4.3b}$$

where f_A and f_B stand for real-valued nonlinear terms which are of the form

$$f_A(t, A, B) = \sum_{n=2}^{\infty} \sum_{j=0}^{n} \sum_{m\in\mathbb{Z}} f_{A,n,j,m} A^j B^{n-j} e^{2im\pi t/T} e^{i(n-1)\pi t/T}$$

and similarly for f_B, where $f_{A,n,j,m}$ and $f_{B,n,j,m}$ are independent of time. To simplify notations, we introduce here the normalized small parameter $\widetilde{\varepsilon}$ for the distance of the two Floquet exponents from the imaginary axis. According to the expansion (2.13), we have

$$\widetilde{\varepsilon} = \varepsilon \frac{\sqrt{2}}{\sqrt{|\lambda''(\ell_0)|}} + \mathcal{O}(\varepsilon^2). \tag{4.4}$$

For analyzing (4.3) we simplify this system by eliminating a number of terms by another normal form transformation

LEMMA 4.1. *There exists an $\tilde{\varepsilon}_0 > 0$ such that for all $\tilde{\varepsilon} \in (0, \tilde{\varepsilon}_0)$ there exists a change of coordinates*

$$A = A_3 + F_A(A_3, B_3), \qquad B = B_3 + F_B(A_3, B_3),$$

with F_A and F_B polynomials not containing linear terms, such that system (4.3a)-(4.3b) transforms into

$$\dot{A}_3 = B_3 + f_{A,3,3,-1,2} A_3^3 + f_{A,3,2,-1,2} A_3^2 B_3 + f_{A,3,1,-1,2} A_3 B_3^2 + f_{A,3,0,-1,2} B_3^3 + \mathcal{O}(|A_3|^4 + |B_3|^4),$$
$$\dot{B}_3 = \widetilde{\varepsilon}^2 A_3 + f_{B,3,3,-1,2} A_3^3 + f_{B,3,2,-1,2} A_3^2 B_3 + f_{B,3,1,-1,2} A_3 B_3^2 + f_{B,3,0,-1,2} B_3^3 + \mathcal{O}(|A_3|^4 + |B_3|^4),$$

with real-valued coefficients $f_{A,n,j,m,2}$ and $f_{B,n,j,m,2}$.

Proof. It is well known that all terms which have a pre-factor which is oscillating in time can be eliminated by a normal form transform or equivalently by averaging, cf. [18, 40]. The technique is elaborated in the Normal Form Theorem III of [22, Theorem III.13]. For the quadratic terms there is no term which has a pre-factor which is constant in time and so all quadratic terms can be eliminated by a transformation

$$A = A_2 + \sum_{j=0}^{2} \sum_{m\in\mathbb{Z}} g_{A,2,j,m,1} A_2^j B_2^{2-j} e^{2im\pi t/T} e^{i\pi t/T},$$
$$B = B_2 + \sum_{j=0}^{2} \sum_{m\in\mathbb{Z}} g_{B,2,j,m,1} A_2^j B_2^{2-j} e^{2im\pi t/T} e^{i\pi t/T}.$$

By suitably choosing the coefficients $g_{A,2,j,m,1}$ and $g_{B,2,j,m,1}$ we find

$$\dot{A}_2 = B_2 + \sum_{n=3}^{\infty}\sum_{j=0}^{n}\sum_{m\in\mathbb{Z}} f_{A,n,j,m,1} A_2^j B_2^{n-j} e^{2im\pi t/T} e^{i(n-1)\pi t/T},$$

$$\dot{B}_2 = \widetilde{\varepsilon}^2 A_2 + \sum_{n=3}^{\infty}\sum_{j=0}^{n}\sum_{m\in\mathbb{Z}} f_{B,n,j,m,1} A_2^j B_2^{n-j} e^{2im\pi t/T} e^{i(n-1)\pi t/T},$$

with new time-independent coefficients $f_{A,n,j,m,1}$ and $f_{B,n,j,m,1}$. For simplifying the cubic terms we make a near identity transformation

$$A_2 = A_3 + \sum_{j=0}^{3}\sum_{m\in\mathbb{Z}} g_{A,3,j,m,2} A_3^j B_3^{3-j} e^{2im\pi t/T},$$

$$B_2 = B_3 + \sum_{j=0}^{3}\sum_{m\in\mathbb{Z}} g_{B,3,j,m,2} A_3^j B_3^{3-j} e^{2im\pi t/T}.$$

Again by suitably choosing the coefficients $g_{A,3,j,m,2}$ and $g_{B,3,j,m,2}$ we find

$$\begin{aligned}\dot{A}_3 &= B_3 + f_{A,3,3,-1,2}A_3^3 + f_{A,3,2,-1,2}A_3^2 B_3 + f_{A,3,1,-1,2}A_3 B_3^2 + f_{A,3,0,-1,2}B_3^3 \\ &\quad + \sum_{n=4}^{\infty}\sum_{j=0}^{n}\sum_{m\in\mathbb{Z}} f_{A,n,j,m,2} A_3^j B_3^{n-j} e^{2im\pi t/T} e^{i(n-1)\pi t/T},\\ \dot{B}_3 &= \widetilde{\varepsilon}^2 A_3 + f_{B,3,3,-1,2}A_3^3 + f_{B,3,2,-1,2}A_3^2 B_3 + f_{B,3,1,-1,2}A_3 B_3^2 + f_{B,3,0,-1,2}B_3^3 \\ &\quad + \sum_{n=4}^{\infty}\sum_{j=0}^{n}\sum_{m\in\mathbb{Z}} f_{B,n,j,m,2} A_3^j B_3^{n-j} e^{2im\pi t/T} e^{i(n-1)\pi t/T},\end{aligned}$$

with new coefficients $f_{A,n,j,m,2}$ and $f_{B,n,j,m,2}$. ∎

5. Proof of Theorem 1.1. Here we obtain the oscillating homoclinic solutions with small tails for $c = 0$. The bifurcating solutions scale as $A_3(t) = \widetilde{\varepsilon}\widetilde{A}(\tau)$ and $B_3(t) = \widetilde{\varepsilon}^2\widetilde{B}(\tau)$, with $\tau = \widetilde{\varepsilon}t$. For the rescaled variables we find

$$\partial_\tau \widetilde{A} = \widetilde{B} + \mathcal{O}(\widetilde{\varepsilon}), \tag{5.1a}$$

$$\partial_\tau \widetilde{B} = \widetilde{A} + f_{B,3,3,-1,2}\widetilde{A}^3 + \mathcal{O}(\widetilde{\varepsilon}). \tag{5.1b}$$

Ignoring the terms of order $\mathcal{O}(\widetilde{\varepsilon})$ we find two homoclinic solutions to the origin, see the left panel of Figure 5.1, if the following sign condition holds.

(Coeff) *Assume that*

$$f_{B,3,3,-1,2} < 0.$$

Remark 5.1. It is shown in Section 7 that **(Coeff)** can generally be satisfied either at the bifurcation (2.10) or (2.11).

Remark 5.2. The truncated system (5.1), with $\mathcal{O}(\widetilde{\varepsilon})$ terms neglected, admits an explicit solution

$$\begin{cases} \widetilde{A}_{\mathrm{hom},0}(\tau) = \sqrt{2|f_{B,3,3,-1,2}|^{-1}}\,\mathrm{sech}(\tau-\tau_0), \\ \widetilde{B}_{\mathrm{hom},0}(\tau) = -\sqrt{2|f_{B,3,3,-1,2}|^{-1}}\tanh(\tau-\tau_0)\mathrm{sech}(\tau-\tau_0), \end{cases} \tag{5.2}$$

where $f_{B,3,3,-1,2} < 0$ and $\tau_0 \in \mathbb{R}$ is to our disposal.

In the invariant subspace $\{W_{h,M} = 0\}$ the homoclinic orbits persist in the reduced system (4.1) if the following reversibility condition holds.

(Rev) *Assume that there exists* $t_0 \in [0, T]$ *such that* $k(t - t_0) = k(t_0 - t)$.

Remark 5.3. Condition **(Rev)** is satisfied for $k(t)$ defined in (1.5) with either $t_0 = \frac{1}{2}\tau_d T$ or $t_0 = \frac{1}{2}(\tau_d + 1)T$. There exist many other possible time-periodic coefficients $k(t)$ satisfying the reversibility condition (5.3) which lead to the same kind of solutions as in Theorems 1.1.

As a consequence of the reversibility, if $t \mapsto (\widetilde{A}(t), \widetilde{B}(t))$ is a solution, so is

$$t \mapsto (\widetilde{A}(2t_0 - t), -\widetilde{B}(2t_0 - t)).$$

Hence, the one-dimensional unstable manifold of the origin of the time $2T$-mapping transversely intersects the fixed space of reversibility $\{(\widetilde{A}, \widetilde{B}) : \widetilde{B} = 0\}$ and continue from the upper half to the lower half of the phase plane, see the right panel of Figure 5.1. Hence, by extending $(\widetilde{A}(t), \widetilde{B}(t))_{t \le t_0}$ by its mirror picture $(\widetilde{A}(2t_0 - t), -\widetilde{B}(2t_0 - t))_{t \ge t_0}$ at the fixed space of reversibility we constructed a homoclinic orbit

$$(A, B)(t) = (\widetilde{\varepsilon}\widetilde{A}_{\rm hom}(\varepsilon t), \widetilde{\varepsilon}^2 \widetilde{B}_{\rm hom}(\widetilde{\varepsilon} t))$$

for the reduced system (4.3), where $\widetilde{A}_{\rm hom} = \widetilde{A}_{\rm hom,0} + \mathcal{O}(\widetilde{\varepsilon})$ and $\widetilde{B}_{\rm hom} = \widetilde{B}_{\rm hom,0} + \mathcal{O}(\widetilde{\varepsilon})$ with the leading-order solution given by (5.2). In the original variables the homoclinic orbit is denoted with $\mathcal{W}$ and corresponds to the truncation $W_{h,M} = 0$ for a given $M \in \mathbb{N}$.

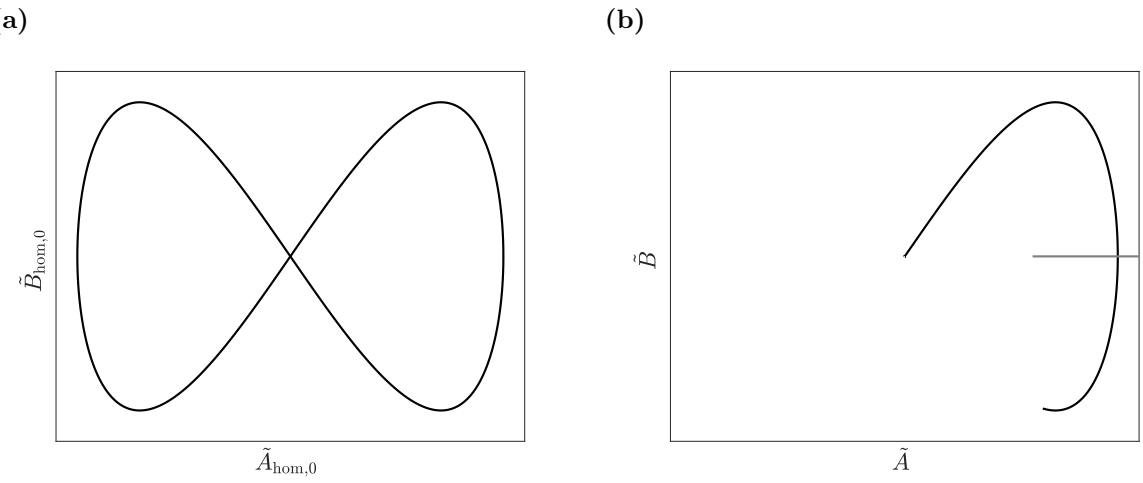

FIG. 5.1. ***(a)*** *Two homoclinic solutions of Eq.* (5.1) *with* $\mathcal{O}(\widetilde{\varepsilon})$ *terms neglected.* ***(b)*** *A sketch of the transversal intersection of the unstable manifold with the fixed space of reversibility.*

The rest of this section contains the proof of Theorem 1.1, which we rewrite in notations of Sections 3 and 4 as follows.

THEOREM 5.4. *Assume the validity of* **(Spec)**, **(Coeff)**, *and* **(Rev)**. *Then there exists an* $\widetilde{\varepsilon}_0 > 0$ *and* $C_0 > 0$ *such that for all* $\widetilde{\varepsilon} \in (0, \widetilde{\varepsilon}_0)$ *and every* $M \in \mathbb{N}$ *with* $M \ge 3$ *the system* (3.8)-(3.9) *possesses a generalized homoclinic solution* $W_{\rm hom} : [-\widetilde{\varepsilon}^{-M+2}, \widetilde{\varepsilon}^{-M+2}] \to \mathbb{R}^{2N}$ *with*

$$\sup_{t \in [-\widetilde{\varepsilon}^{-M+2}, \widetilde{\varepsilon}^{-M+2}]} \| W_{\rm hom}(t) - \mathcal{W}(t) \| \le C_0 \widetilde{\varepsilon}^{M-1}$$

with $\lim_{|t|\to\infty} \mathcal{W}(t) = 0$. *Moreover, for* $\mathcal{W}(t) = (\mathcal{W}_0(t), \mathcal{W}_h(t))$ *we have*

$$\sup_{t\in[-\widetilde{\varepsilon}^{-M+2},\widetilde{\varepsilon}^{-M+2}]} \|\mathcal{W}_h(t)\| \le C_0\widetilde{\varepsilon}^2$$

and

$$\sup_{t\in[-\widetilde{\varepsilon}^{-M+2},\widetilde{\varepsilon}^{-M+2}]} \|\mathcal{W}_0(t) - \widetilde{\varepsilon}A_{\mathrm{hom},0}(\widetilde{\varepsilon}^2 t)\varphi_1\| \le C_0\widetilde{\varepsilon}^2,$$

with $A_{\mathrm{hom},0}$ *given by* (5.2).

Proof. To prove persistence of $\mathcal{W}$ if the terms $H_M(W_0) = \mathcal{O}(\|W_0\|^M)$ are taken into account, we use again the reversibility. Obviously, it is impossible that the one-dimensional unstable manifold transversally intersects the N-dimensional fixed space of reversibility for the full system (3.10)-(3.11). Therefore, it can only be expected that the homoclinic solutions persist as solutions with small tails for $|t| \to \infty$. This can rigorously be shown by intersecting the $2N-1$-dimensional center-unstable manifold with the fixed space of reversibility. Obviously this intersection is a transversal intersection.

On the center-unstable manifold the solutions converge towards the center manifold for $t \to -\infty$ with some exponential rate. However, the solutions on the center manifold can grow slowly, hence it remains to obtain bounds for such solutions. In a first step we apply another normal form transformation

$$W_{0,M} = \widetilde{W}_{0,M} + Q_0(W_0, W_{h,M}), \qquad W_{h,M} = \widetilde{W}_{h,M} + Q_h(W_0, W_{h,M})$$

to eliminate the bilinear terms which are linear in W_0 and linear in $W_{h,M}$ from the full system (3.10)-(3.11), where the

$$Q_{0,h}(W_0, W_{h,M}) = \sum_{m\in\mathbb{Z}} Q_{0,h}(W_0, W_{h,M})[m]e^{2im\pi t/T}e^{i\pi t/T}$$

are bilinear mappings in their arguments. With some slight abuse of notation we skip the tildes and reconsider the system (3.10)-(3.11) but now with $N_{0,M}$ and $N_{h,M}$ additionally satisfying

$$\begin{aligned} \|N_{0,M}(W_0, W_{h,M})\| &\le C(\|W_0\|^3 + \|W_0\|^2\|W_{h,M}\| + \|W_{h,M}\|^2), \\ \|N_{h,M}(W_0, W_{h,M})\| &\le C(\|W_0\|^2\|W_{h,M}\| + \|W_{h,M}\|^2). \end{aligned}$$

The transformations are possible due to the spectral assumption **(Spec)**.

In a second step we introduce the deviation $\widetilde{W}_0$ from the homoclinic orbit $\mathcal{W}_0$ by $W_0 = \mathcal{W}_0 + \widetilde{W}_0$. The subsequent estimates on the deviation $\widetilde{W}_0$ have already been carried out in a number of papers, cf. [17, 10]. We use the cutoff functions to estimate the solutions on $[-\xi_0, \xi_0]$ with a suitable chosen large ξ_0 as $\tilde{\varepsilon} \to 0$.

The homoclinic orbit can be estimated pointwise by $\|\mathcal{W}_0(t)\| \le \widetilde{\varepsilon}q(\widetilde{\varepsilon}t)$ with a smooth $q \in L^1(\mathbb{R})$. We denote the stable part of $\widetilde{W}_0$ by $\widetilde{W}_{0,s}$ and the projection on the stable part by Π_s. We find for a large ξ_0 determined below that

$$\begin{aligned} \|\widetilde{W}_{0,s}(t)\| &= \left\| \int_{-\xi_0}^{t} e^{\Lambda_0(t-\tau)}\Pi_0 \left[N_{0,M}(\mathcal{W}_0 + \widetilde{W}_0, W_{h,M}) - N_{0,M}(\mathcal{W}_0, 0) \right](\tau) d\tau \right\| \\ &\le CY(t) \int_{-\infty}^{t} e^{-\widetilde{\varepsilon}(t-\tau)}\widetilde{\varepsilon}^2 q^2(\widetilde{\varepsilon}\tau) d\tau + CY(t)^2 \int_{-\infty}^{t} e^{-\widetilde{\varepsilon}(t-\tau)} d\tau \\ &\le C\widetilde{\varepsilon}Y(t) + C\widetilde{\varepsilon}^{-1}Y(t)^2, \end{aligned}$$

where

$$Y(t) := \sup_{\tau\in[-\xi_0,t]} (\|\widetilde{W}_0(\tau)\| + \|W_{h,M}(\tau)\|).$$

If the solution is in the fixed space of reversibility at $t = 0$ we find

$$\begin{aligned}\|W_{h,M}(t)\| &= \left\| \int_0^t e^{\Lambda_h(t-\tau)}(N_{h,M}(W_0, W_{h,M})(\tau) + H_M(W_0)(\tau))d\tau \right\| \\ &\leq CY(t)\int_0^t \widetilde{\varepsilon}^2 q^2(\widetilde{\varepsilon}\tau)d\tau + C|t|Y(t)^2 + C\int_0^t \widetilde{\varepsilon}^M q^M(\widetilde{\varepsilon}\tau)d\tau \\ &\leq C\widetilde{\varepsilon}Y(t) + C|t|Y(t)^2 + C\widetilde{\varepsilon}^{M-1}.\end{aligned}$$

Summarizing the estimates yields

$$Y(\xi_0) \leq C\widetilde{\varepsilon}Y(\xi_0) + C\widetilde{\varepsilon}^{-1}Y(\xi_0)^2 + C|\xi_0|Y(\xi_0)^2 + C\widetilde{\varepsilon}^{M-1}$$

and so $Y(\xi_0) \leq C\varepsilon^{M-1}$ for $\xi_0 \leq \widetilde{C}\varepsilon^{-M+2}$ and $M \geq 3$. This completes the proof of the theorem in view of the normal form transformations. ∎

6. Proof of Theorem 1.2 and Theorem 1.3. Here we consider the case of small damping $c > 0$ where reversibility no longer holds. For consistency of our analysis, we assume that $c = \widetilde{c}\widetilde{\varepsilon}$ with $\widetilde{c} = \mathcal{O}(1) > 0$ fixed. With the same analysis as for (4.3) and (5.1) we end up in $\{W_{h,M} = 0\}$ at the reduced system for the rescaled variables which is now given by

$$\partial_\tau \widetilde{A} = \widetilde{B} + \mathcal{O}(\widetilde{\varepsilon}), \tag{6.1a}$$

$$\partial_\tau \widetilde{B} = \widetilde{A} - \frac{\widetilde{c}}{\underline{m}}\widetilde{B} + f_{B,3,3,-1,2}\widetilde{A}^3 + \mathcal{O}(\widetilde{\varepsilon}), \tag{6.1b}$$

where we used the expression $\gamma = \upsilon - \frac{c}{2\underline{m}}$ for the Floquet exponents of the mapping (2.6) in Section 2.1. Ignoring the terms of order $\mathcal{O}(\widetilde{\varepsilon})$ we first find two fixed points $(\widetilde{A}, \widetilde{B})_\pm = (\pm 1/\sqrt{|f_{B,3,3,-1,2}|}, 0)$ if $f_{B,3,3,-1,2} < 0$. Since the fixed points are hyperbolic they persist as fixed points of the time-$2T$-mapping even if the terms of order $\mathcal{O}(\widetilde{\varepsilon})$ are included. This proves Theorem 1.2.

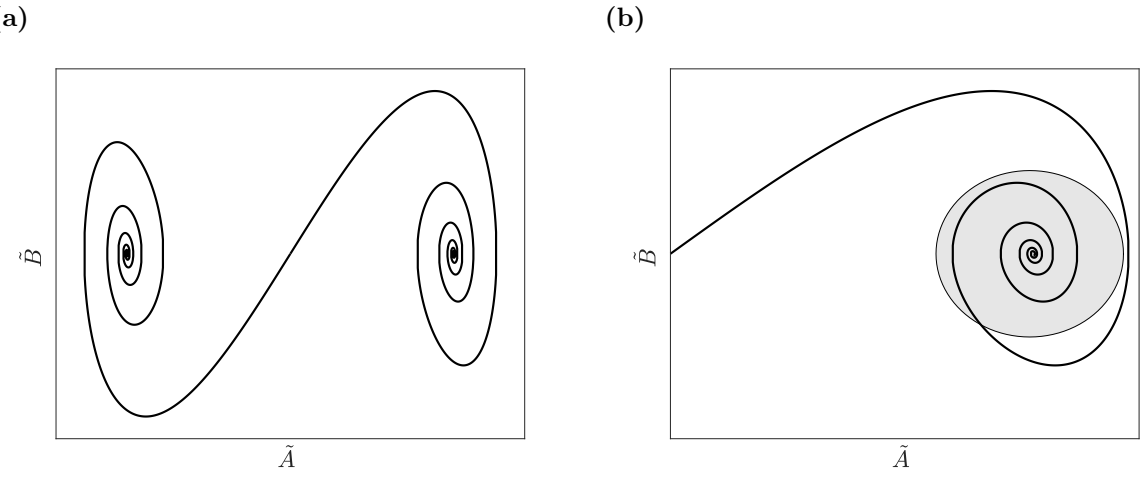

FIG. 6.1. ***(a)*** *Two heteroclinic solutions for small $c > 0$ of Eq. (6.1) with $\mathcal{O}(\widetilde{\varepsilon})$ terms neglected.* ***(b)*** *The heteroclinic solution of Eq. (6.1) in the intersection of the one-dimensional unstable manifold from the zero equilibrium point (in black) and the stable manifold from the positive fixed point (in gray).*

Next we find two heteroclinic solutions connecting the origin with the two fixed points $(\widetilde{A}, \widetilde{B})_\pm$. In order to prove the persistence of these heteroclinic solutions we use that the one-dimensional unstable manifold

of the origin transversely intersects the two-dimensional stable manifold of the two other fixed points of the reduced system. These heteroclinic solutions are shown on Figure 6.1.

To prove the persistence of heteroclinic solutions if the terms $H_M(W_0) = \mathcal{O}(|W_0|^M)$ are taken into account we use that the stable manifold of the two other fixed points is $2N$-dimensional and so the one-dimensional unstable manifold of the origin transversally intersects the $2N$-dimensional stable manifold of the two anti-periodic solutions from Theorem 1.2. Theorem 1.3 is proven by using the transformations of Sections 3 and 4, with the decomposition $W = (W_0, W_h)$.

7. Multiple-scale analysis and checking the assumption (Coeff). For the system (1.1) with (1.2) we already checked the spectral condition **(Spec)** used in Theorems 1.1-1.3. Here we establish the validity of the normal form coefficient condition **(Coeff)**.

We do so by formally deriving the reduced systems (5.1) and (6.1) via a multiple-scale analysis, which will yield an explicit and convenient formula for $f_{B,3,3,-1,2}$ after adjusting the notations. Truncating (6.1) with $\mathcal{O}(\widetilde{\varepsilon})$ terms neglected yields the scalar equation:

$$\partial_\tau^2 \widetilde{A} + \frac{\widetilde{c}}{\underline{m}} \partial_\tau \widetilde{A} = \widetilde{A} + f_{B,3,3,-1,2} \widetilde{A}^3 \tag{7.1}$$

Remark 7.1. The scalar equation (7.1) is recovered in Eq. (7.18) below with the correspondence between ε and $\widetilde{\varepsilon}$ given by (4.4). Note that the definition $A = \widetilde{\varepsilon} \widetilde{A}(\widetilde{\varepsilon} t)$, see Eq. (4.2), is different from the definition $A(\varepsilon t)$, see Eq. (7.13) below. For Eq. (7.1), the amplitude $\widetilde{A}$ is introduced based on the Floquet theorem, the decomposition into subspaces, and the normal form transformations. For Eq. (7.18), the amplitude A is introduced directly by the perturbation expansions in powers of ε, see Eq. (7.12).

We define as in (2.12),

$$k(t) = k_0(t) + \delta \varepsilon^2, \tag{7.2}$$

where $k_0(t)$ is the potential for the bifurcation (2.10) or (2.11), ε is a small parameter for the asymptotic expansion, and δ is a proper sign factor.

7.1. Bloch modes of the unperturbed linear problem. We start with the linear problem for $c = 0$. In order to construct the asymptotic expansion, we define the Bloch function $v(t) = e^{i\ell t} f_j(\ell, t)$ for the j-th spectral band $\lambda_j(\ell)$ of $\mathcal{L}_0 v = \lambda v$, where $f_j(\ell, t + T) = f_j(\ell, t)$. The parameter ℓ is defined in the Brillouin zone $[0, \frac{2\pi}{T})$ with $\ell = 0$ and $\ell = \frac{\pi}{T}$ being at the ends of each spectral band corresponding to periodic and anti-periodic solutions respectively.

Let $L^2_{\rm per}$ be the Hilbert space of 2π-periodic functions with the inner product $\langle \cdot, \cdot \rangle$ and the induced norm $\| \cdot \|_{L^2_{\rm per}}$. The $L^2_{\rm per}$-normalized Bloch function $f_j(\ell, t)$ is a T-periodic solution of the spectral problem

$$\left[-\underline{m}(\partial_t + i\ell)^2 - k_0(t) \right] f_j(\ell, t) = \lambda_j(\ell) f_j(\ell, t), \tag{7.3}$$

which can be differentiated in ℓ as

$$\left[-\underline{m}(\partial_t + i\ell)^2 - k_0(t) - \lambda_j(\ell) \right] \partial_\ell f_j(\ell, t) = 2i\underline{m}(\partial_t + i\ell) f_j(\ell, t) + \lambda_j'(\ell) f_j(\ell, t) \tag{7.4}$$

and

$$\begin{aligned} \left[-\underline{m}(\partial_t + i\ell)^2 - k_0(t) - \lambda_j(\ell) \right] \partial_\ell^2 f_j(\ell, t) &= 4i\underline{m}(\partial_t + i\ell) \partial_\ell f_j(\ell, t) \\ &+ 2\lambda_j'(\ell) \partial_\ell f_j(\ell, t) + \left[\lambda_j''(\ell) - 2\underline{m} \right] f_j(\ell, t), \end{aligned} \tag{7.5}$$

Projecting to $f(\ell,t)$ in $L^2_{\rm per}$ yields from (7.4) and (7.5):

$$\lambda_j'(\ell) = -2\underline{m}\langle f_j(\ell,\cdot), i\partial_t f_j(\ell,\cdot)\rangle + 2\underline{m}\ell, \tag{7.6}$$

and

$$\begin{aligned}\lambda_j''(\ell) + 2\lambda_j'(\ell)\langle f_j(\ell,\cdot), \partial_\ell f_j(\ell,\cdot)\rangle &= -4\underline{m}\langle f_j(\ell,\cdot), i\partial_t\partial_\ell f_j(\ell,\cdot)\rangle \\ &+ 4\underline{m}\langle f_j(\ell,\cdot), \partial_\ell f_j(\ell,\cdot)\rangle\langle f_j(\ell,\cdot), i\partial_t f_j(\ell,\cdot)\rangle + 2\underline{m},\end{aligned} \tag{7.7}$$

where the normalization condition $\|f_j(\ell,\cdot)\|_{L^2_{\rm per}} = 1$ has been used.

Remark 7.2. If $\ell_0 = \frac{\pi}{T}$ for the bifurcating mode and the band gap (μ_1,μ_2) has a non-zero width, then necessarily, $\lambda_j'(\ell_0) = 0$. If the bifurcation (2.10) occurs at μ_1, then $j = 1$ and $\lambda_1''(\ell_0) < 0$. See Fig. 2.1(c) for an example. If the bifurcation (2.11) occurs at μ_2, then $j = 2$ and $\lambda_2''(\ell_0) > 0$. See Fig. 8.3(a).

7.2. Perturbation of the linear problem. Let us consider asymptotic solutions of the linear equation

$$(\mathcal{L}_0 - K_2\omega^2(q_{m_0}) - \delta\varepsilon^2)\widehat{u}(t) = 0, \tag{7.8}$$

which follows from (2.2) and (7.2) at $m = m_0$. As in (2.10), we take $\mu_1 = K_2\omega^2(q_{m_0})$ for which $\ell_0 = \frac{\pi}{T}$ is selected in the first spectral band $\{\lambda_1(\ell)\}_{\ell\in[0,\frac{2\pi}{T})}$. The set-up for the second spectral band $\{\lambda_2(\ell)\}_{\ell\in[0,\frac{2\pi}{T})}$ when $\mu_2 = K_2\omega^2(q_{m_0})$ as in (2.11) is essentially identical (see remark 7.3). Expanding

$$\widehat{u}(t) = A(\varepsilon t)e^{i\ell_0 t}f_1(\ell_0,t) + \varepsilon B(\varepsilon t)e^{i\ell_0 t}g_1(\ell_0,t) + \varepsilon^2 e^{i\ell_0 t}C(\varepsilon t)h_1(\ell_0,t) + \mathcal{O}(\varepsilon^3),$$

with A, B, C and g_1, h_1 to be determined, we obtain for $\mu_1 = K_2\omega^2(q_{m_0})$ at the order of $\mathcal{O}(\varepsilon)$ that

$$B\left[-\underline{m}(\partial_t + i\ell_0)^2 - k_0(t) - \mu_1\right] g_1(\ell_0,t) = 2mA'(\partial_t + i\ell_0)f_1(\ell_0,t),$$

Since $\lambda_1(\ell_0) = \mu_1$ and $\lambda_1'(\ell_0) = 0$, comparing with (7.4) yields

$$g_1(t) = \partial_\ell f_1(\ell_0,t) \quad \text{and} \quad B(\varepsilon t) = -iA'(\varepsilon t).$$

At the order of $\mathcal{O}(\varepsilon^2)$, we obtain the linear inhomogeneous equation,

$$\begin{aligned}C\left[-\underline{m}(\partial_t + i\ell_0)^2 - k_0(t) - \mu_1\right] h_1(t) &= -2\underline{m}iA''(\partial_t + i\ell_0)\partial_\ell f_1(\ell_0,t) \\ &+ \underline{m}A'' f_1(\ell_0,t) + \delta A f_1(\ell_0,t).\end{aligned} \tag{7.9}$$

Comparing (7.9) with (7.5) yields $h_1(t) = \partial_\ell^2 f_1(\ell_0,t)$ and $C(\varepsilon t) = -\frac{1}{2}A''(\varepsilon t)$ if and only if $A(\tau)$, $\tau := \varepsilon t$ satisfies the amplitude equation

$$\frac{1}{2}\lambda_1''(\ell_0)A''(\tau) + \delta A(\tau) = 0. \tag{7.10}$$

Alternatively, the amplitude equation (7.10) can be obtained by projecting the linear inhomogeneous equation (7.9) to $f_1(\ell_0,t)$ in $L^2_{\rm per}$ and using equations (7.6) and (7.7) with $\lambda_1'(\ell_0) = 0$.

Since δ and $\lambda_1''(\ell_0)$ have opposite signs, $A(\tau)$ of Eq. (7.10) will experience exponential growth with rate

$$\varepsilon\frac{\sqrt{2}}{\sqrt{|\lambda_1''(\ell_0)|}}, \tag{7.11}$$

which is the leading order for Eq. (4.4). This is an approximation of the real part of the Floquet exponent associated to the m_0-th mode of the linear problem with $k(t) = k_0(t) + \delta\varepsilon^2$, see Eq. (2.13) and Fig. 8.1(c) for example.

Remark 7.3. If $\lambda_1''(\ell_0) < 0$ for the bifurcating mode (2.10), then $\delta = +1$ is selected from the condition that $\mu_1 = K_2\omega^2(q_{m_0})$ is inside the band gap of the perturbed operator $\mathcal{L} = \mathcal{L}_0 - \delta\varepsilon^2$. On the other hand, if $\lambda_2''(\ell_0) > 0$ for the bifurcating mode (2.11), then $\delta = -1$ is selected from the condition that $\mu_2 = K_2\omega^2(q_{m_0})$ is inside the band gap of $\mathcal{L}$.

7.3. Perturbation of the nonlinear problem. Let us now consider asymptotic solutions of the nonlinear equation (1.1) with (7.2) and $c = \varepsilon\tilde{c}$, where $\tilde{c} \geq 0$ is fixed and $\delta = -\text{sign}(\lambda_1''(\ell_0))$. As in (2.10), we take $\mu_1 = K_2\omega^2(q_{m_0})$, for which $\ell_0 = \frac{\pi}{T}$ is selected in the first spectral band $\{\lambda_1(\ell)\}_{\ell\in[0,\frac{2\pi}{T})}$. To simplify computations, we will use expansions in terms of real-valued functions only. Expanding

$$u_n(t) = \varepsilon U_n^{(1)}(t) + \varepsilon^2 U_n^{(2)}(t) + \varepsilon^3 U_n^{(3)}(t) + \mathcal{O}(\varepsilon^4), \tag{7.12}$$

we select the leading order in the form

$$U_n^{(1)}(t) = A(\varepsilon t) g_1(t) \sin(q_{m_0} n), \tag{7.13}$$

where the amplitude $A(\varepsilon t)$ is real according to (7.1) and the eigenfunction

$$g_1(t) := \left[e^{i\ell_0 t} f_1(\ell_0, t) + e^{-i\ell_0 t}\bar{f}_1(\ell_0, t)\right] \tag{7.14}$$

is a real-valued, T-anti-periodic solution of $\mathcal{L}_0 g_1 = \mu_1 g_1$ satisfying $g_1(t+T) = -g_1(t)$. At the order of $\mathcal{O}(\varepsilon^2)$ we obtain

$$\mathcal{L}_0 U_n^{(2)} + K_2(U_{n+1}^{(2)} - 2U_n^{(2)} + U_{n-1}^{(2)}) = H_n^{(2)},$$

with

$$H_n^{(2)} = 2\underline{m}\partial_\tau\partial_t U_n^{(1)} + \tilde{c}\partial_t U_n^{(1)} + K_3\left[(U_{n+1}^{(1)} - U_n^{(1)})^2 - (U_n^{(1)} - U_{n-1}^{(1)})^2\right],$$

where $\tau = \varepsilon t$ and K_3 is the coefficient of the quadratic term in (1.1). In the explicit form, we obtain

$$H_n^{(2)} = [2\underline{m}A'(\tau) + \tilde{c}A(\tau)] g_1'(t)\sin(q_{m_0} n) + K_3 A(\tau)^2 g_1(t)^2 F_n^{(2)},$$

with

$$\begin{aligned} F_n^{(2)} &= [\sin(q_{m_0}(n+1)) - \sin(q_{m_0} n)]^2 - [\sin(q_{m_0} n) - \sin(q_{m_0}(n-1))]^2 \\ &= -2\sin(q_{m_0})(1 - \cos(q_{m_0}))\sin(2q_{m_0} n). \end{aligned}$$

The solution for $U_n^{(2)}(t)$ can be written in the form

$$U_n^{(2)}(t) = \left[A'(\tau) + \frac{\tilde{c}}{2\underline{m}}\right] h_1(t)\sin(q_{m_0} n) + K_3 A(\tau)^2 h_2(t)\sin(2q_{m_0} n),$$

where h_1 and h_2 are solutions of the linear inhomogeneous equations:

$$(\mathcal{L}_0 - K_2\omega^2(q_{m_0}))h_1 = 2\underline{m} g_1'(t), \tag{7.15}$$

$$(\mathcal{L}_0 - K_2\omega^2(2q_{m_0}))h_2 = -2\sin(q_{m_0})(1 - \cos(q_{m_0}))g_1(t)^2. \tag{7.16}$$

It follows from the linear theory that the real, T-anti-periodic solution for $h_1(t)$ exists in the form:

$$h_1(t) = -ie^{i\ell_0 t}\partial_\ell f_1(\ell_0, t) + ie^{-i\ell_0 t}\partial_\ell \bar{f}_1(\ell_0, t).$$

There exists a unique T-periodic solutions for $h_2(t)$ if and only if the non-resonance condition is met:

$$K_2\omega^2(2q_{m_0}) \notin \cup_{j=1}^{\infty}\lambda_j(0). \tag{7.17}$$

This non-resonance condition is satisfied if the spectral assumption (**Spec**) is satisfied.

At the order of $\mathcal{O}(\varepsilon^3)$, we obtain

$$\mathcal{L}_0 U_n^{(3)} + K_2(U_{n+1}^{(3)} - 2U_n^{(3)} + U_{n-1}^{(3)}) = H_n^{(3)},$$

with

$$\begin{aligned} H_n^{(3)} &= \delta U_n^{(1)} + 2m\partial_\tau \partial_t U_n^{(2)} + m\partial_\tau^2 U_n^{(1)} + \tilde{c}\partial_t U_n^{(2)} + \tilde{c}\partial_\tau U_n^{(1)} \\ &\quad + 2K_3\left[(U_{n+1}^{(1)} - U_n^{(1)})(U_{n+1}^{(2)} - U_n^{(2)}) - (U_n^{(1)} - U_{n-1}^{(1)})(U_n^{(2)} - U_{n-1}^{(2)})\right] \\ &\quad - K_4\left[(U_{n+1}^{(1)} - U_n^{(1)})^3 - (U_n^{(1)} - U_{n-1}^{(1)})^3\right], \end{aligned}$$

where K_4 is the coefficient of the cubic term in (1.1).

By using Euler's formulas, we obtain

$$\begin{aligned} &[\sin(q_{m_0}(n+1)) - \sin(q_{m_0}n)]^3 - [\sin(q_{m_0}n) - \sin(q_{m_0}(n-1))]^3 \\ &\quad = -3(1-\cos(q_{m_0}))^2 \sin(q_{m_0}n) \\ &\qquad + \frac{1}{2}\left[1 - 3\cos(q_{m_0}) + 3\cos(2q_{m_0}) - \cos(3q_{m_0})\right]\sin(3q_{m_0}n) \end{aligned}$$

and

$$\begin{aligned} &[\sin(q_{m_0}(n+1)) - \sin(q_{m_0}n)]\,[\sin(2q_{m_0}(n+1)) - \sin(2q_{m_0}n)] \\ &\qquad - [\sin(q_{m_0}n) - \sin(q_{m_0}(n-1))]\,[\sin(2q_{m_0}n) - \sin(2q_{m_0}(n-1))] \\ &\quad = -\left[2\sin(q_{m_0}) - \sin(2q_{m_0})\right]\sin(q_{m_0}n) \\ &\qquad - \left[\sin(q_{m_0}) + \sin(2q_{m_0}) - \sin(3q_{m_0})\right]\sin(3q_{m_0}n) \end{aligned}$$

Hence, we obtain

$$H_n^{(3)} = D_1(t)\sin(q_{m_0}n) + D_2(t)\sin(2q_{m_0}n) + D_3(t)\sin(3q_{m_0}n),$$

where we are only interested to write explicitly the coefficient for the bifurcating mode:

$$\begin{aligned} D_1(t) &= \delta A(\tau)g_1(t) + mA''(\tau)g_1(t) + 2mA''(\tau)h_1'(t) \\ &\quad + \tilde{c}\left[A'(\tau)g_1(t) + 2A'(\tau)h_1'(t)\right] + \frac{\tilde{c}^2}{2\underline{m}}A(\tau)h_1'(t) \\ &\quad + 3K_4(1-\cos(q_{m_0}))^2 A(\tau)^3 g_1(t)^3 - 2K_3^2\left[2\sin(q_{m_0}) - \sin(2q_{m_0})\right]A(\tau)^3 g_1(t)h_2(t). \end{aligned}$$

Projecting $D_1(t)$ to $g_1(t)$ gives the amplitude equation for $A(\tau)$:

$$\frac{1}{2}\lambda_1''(\ell_0)\left[A''(\tau) + \frac{\tilde{c}}{\underline{m}}A'(\tau) + \frac{\tilde{c}^2}{4\underline{m}^2}A(\tau)\right] + \left[\delta - \frac{\tilde{c}^2}{4\underline{m}}\right]A(\tau) + \chi A(\tau)^3 = 0, \tag{7.18}$$

where

$$\lambda_1''(\ell_0) = 2m + 4m\frac{\langle g_1, h_1'\rangle}{\|g_1\|^2} \tag{7.19}$$

and

$$\chi = 3K_4(1-\cos(q_{m_0}))^2\frac{\langle g_1^2, g_1^2\rangle}{\|g_1\|^2} - 2K_3^2\left[2\sin(q_{m_0}) - \sin(2q_{m_0})\right]\frac{\langle g_1^2, h_2\rangle}{\|g_1\|^2}. \tag{7.20}$$

Since the linear part of (7.18) should be identical to the linear amplitude equation (7.10), the new formula for $\lambda_1''(\ell_0)$ must be identical to the previous equation (7.7) with $\lambda_1'(\ell_0) = 0$. The expression for χ is defined in terms of real quantities only.

Remark 7.4. Equation (7.18) for $\tilde{c} = 0$ is analogous to the stationary NLS equation that can be derived in the context of spatially periodic media for the description of breathers [21]. A similar equation was derived in [34] for a (space-time continuous) photonic time crystal. Eq. (7.18) is equivalent to (7.1) with the correspondence (4.4) and the appropriate definitions of amplitudes A and $\widetilde{A}$. The coefficient $f_{B,3,3,-1,2}$ is constant proportional to $\chi/\lambda_1''(\ell_0)$.

Remark 7.5. The coefficient in front of the second derivative in the amplitude equation (7.18) comes from an expansion of the imaginary parts of the spectral curves at the spectral gaps, see Fig. 2.1(c). The coefficient in front of the second derivative changes sign at every spectral boundary. Since the coefficient in front of the cubic coefficient in (7.18) does not change sign, the homoclinic and heteroclinic solutions exist as bifurcating solutions at every spectral gap associated with the anti-periodic eigenfunctions. In other words, if $\chi < 0$, then we pick the bifurcating mode at (2.10) with $\lambda_1''(\ell_0) < 0$ and $\delta = +1$. If $\chi > 0$, then we pick the bifurcating mode at (2.11) with $\lambda_2''(\ell_0) > 0$ and $\delta = -1$.

8. Comparison with numerical simulations.

We now conduct a number of numerical simulations to illustrate the main results of the paper. We start with the simplest case, and work up in complexity.

Equation (7.18) with $\tilde{c} = 0$ and $\delta = -\text{sign}(\lambda_1''(\ell_0)) = -\text{sign}(\chi)$ has the following homoclinic solution

$$A(\tau) = \sqrt{\frac{2}{|\chi|}}\,\text{sech}\left(\sqrt{\frac{2}{|\lambda_1''(\ell_0)|}}\tau\right) \tag{8.1}$$

See Fig. 5.1(a) for an example plot of this solution in the (A, A') phase plane. Returning to ansatz Eq. (7.12), we have the following leading order approximation in terms of the original lattice variables,

$$u_n(t) = \varepsilon\sqrt{\frac{2}{|\chi|}}\,\text{sech}\left(\sqrt{\frac{2}{|\lambda_1''(\ell_0)|}}\varepsilon t\right) g_1(t)\sin(q_{m_0}n). \tag{8.2}$$

To make practical use of this approximation, the first step is to identify the bifurcation value k_0 (namely the critical modulation amplitude values k_a^0 and k_b^0) and critical mode number m_0 such that $\text{trace}(J) = -2$ where J is the monodromy matrix defined in Eq. (2.7). This corresponds to the bifurcation scenario shown in Fig. 2.1. In this case, the Floquet exponent corresponding to m_0 will be purely imaginary and will be of the form $i\ell_0 = \frac{i\pi}{T}$. The corresponding Bloch mode $e^{i\ell_0 t}f_1(\ell_0, t)$ is obtained by solving Eq. (7.3). This can be done explicitly, see Sec. 2.1 or the appendix of [7] for details. Next, we compute $\lambda_1''(\ell_0)$ using Eq. (7.7) with $j = 1$ which depends only on f_1 and its derivatives, which can also be computed explicitly. Equivalently, one can determine $\lambda_1''(\ell_0)$ using Eq. (7.19).

8.1. Examples with $c = 0$ and $K_3 = 0$.

The nonlinear coefficient χ can be computed from g_1 if $K_3 = 0$, i.e., if there is no quadratic nonlinearity (the case of $K_3 \neq 0$ is discussed below). To compute χ in this case, we substitute $g_1(t) = 2\text{Re}\left(e^{i\ell_0 t}f_1(\ell_0, t)\right)$ into Eq. (7.20) and evaluate.

As our first example, we chose parameters that correspond to the spectral picture in Fig. 2.1 and $K_3 = 0$ and $K_4 = -0.8$. In this case the critical mode $m_0 = 3$ lies at the top of the first spectral band, namely $(\ell, \lambda) = (\pi/T, \mu_1)$. This demonstrates that the spectral condition **(Spec)** is satisfied and we choose $\delta = +1$. It can be seen from Fig. 2.1(c), or via direct calculation, that $\lambda''(\ell_0) < 0$. By choosing $K_4 < 0$, we have that $\chi < 0$, and thus **(Coeff)** is satisfied.

To generate the generalized q-gap breather, we keep all parameters fixed, but select $\varepsilon = 0.1$ and $k_a = k_a^0 + \varepsilon^2 = 0.06$, $k_b = k_b^0 + \varepsilon^2 = 0.8$. With these parameter values, the $m_0 = 3$ mode lies in the spectral gap. The corresponding Floquet multipliers and exponents and are shown in Fig. 1.1(a,b). We initialize

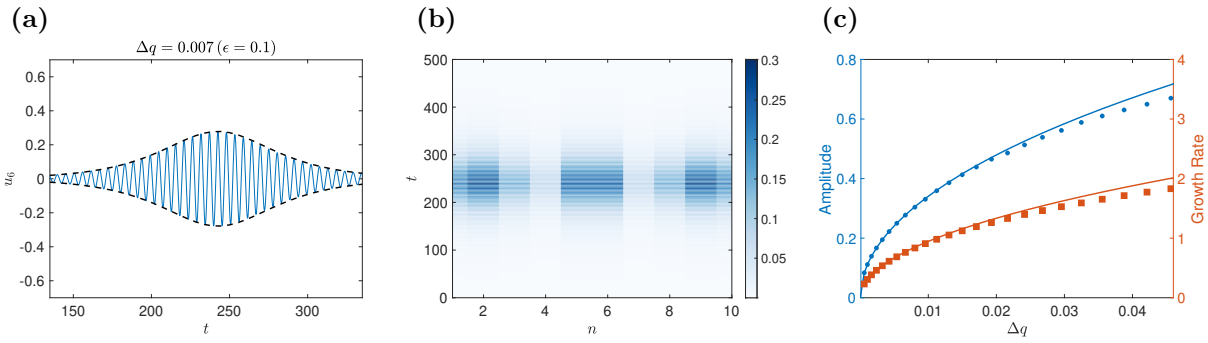

FIG. 8.1. *A generalized q-gap breather bifurcating from μ_1. The parameter values are $c = 0$, $T = 1/0.37$, $K_3 = 0$, $K_4 = -0.8$ and $K_2 = \underline{m} = 1$. The critical modulation amplitude parameters are $k_a^0 = 0.5$ and $k_b^0 = 0.79$. The critical mode number is $m_0 = 3$, which lies at the top of the first spectral band, namely $\lambda(q_3) = \mu_1$, (see Fig. 2.1(a)).* ***(a)*** *Numerical simulation with initial value $u_n(0) = 10^{-4}\sin(q_3 n)$ and $\varepsilon = 0.1$. The displacement of the 6th particle is shown as a function of time. The modulation amplitude is $k_a = k_a^0 + \varepsilon^2 = 0.06$, $k_b = k_b^0 + \varepsilon^2 = 0.8$. The dashed line shows an approximation of the envelope given by Eq. (8.2) with $\chi = -0.6530$, $\lambda''(\ell_0) = -21.0222$ and $\varepsilon = 0.1$. For this value of ε, the distance of the wavenumber to the edge of the gap is $\Delta q = q_3 - q_\ell = 0.007$.* ***(b)*** *Intensity plot of the solution shown in panel (a). Color intensity corresponds to $|u_n|$.* ***(c)*** *Plot of the amplitude of the breather ($\max_t u_6(t)$) for the numerical simulation (blue dots) and prediction based on Eq. (8.2) (blue line) as a function of Δq. The real part of the Floquet exponent corresponding to q_3 (solid red squares) and asymptotic approximation (7.11) (red line) are also shown, which indicate the growth (decay) rate of the breather.*

the numerical simulation with

$$u_n(0) = 10^{-4}\sin(q_3 n) \quad \text{and} \quad \dot{u}_n = 0.$$

For initial data with such small amplitude, the dynamics will initially be nearly linear, and hence the solution will grow exponentially with rate given by $\mathrm{Re}(\gamma)$, which is the real part the Floquet exponent associated to mode $m = 3$ (see the larger black dot in Fig. 1.1(a)). According to Eq. (7.10), an approximation of this growth rate is given by (7.11) with $\varepsilon = 0.1$. As the amplitude increases in the dynamic evolution, the affect of the nonlinearity comes into play, which will cause the solution to experience decay, such that the resulting waveform is localized in time. The time series of the $u_6(t)$ node is shown in Fig. 8.1(a). The temporal localization occurs uniformly throughout the lattice, as seen in the intensity plot of Fig. 8.1(b). By construction, the wavenumber q_3 lies in a wavenumber bandgap. Thus, the solution shown in Fig. 8.1(a,b) is a generalized q-gap breather. The analytical prediction based on Eq. (8.2) is shown as the dashed-line in panel (a). For the sake of clarity, only the envelope of the approximation is shown, which is simply a plot of the local maximums (and minimums) of Eq. (8.2).

For $\varepsilon = 0.1$, the distance of the wavenumber to the edge of the gap is $\Delta q = q_\ell - q_3 = 0.007$, where q_ℓ is the wavenumber at the (left) edge of the gap. Recall from Eq. (2.14) that $\Delta q = \mathcal{O}(\varepsilon^2)$. Since the amplitude of the breather is $\mathcal{O}(\varepsilon)$, see Eq. (8.2), the amplitude grows like $\mathcal{O}(\sqrt{\Delta q})$. This observation was made numerically and experimentally in [7], which we have now proved. This amplitude trend is consistent with the trend found for discrete breathers in space-periodic systems where it is well known that the breather amplitude grows like $\mathcal{O}\left(\sqrt{\Delta\omega}\right)$, where $\Delta\omega$ is the difference between the breather frequency and the edge of the frequency spectrum [12]. Using (2.14) and Eq. (8.2) allows us to obtain an analytical prediction of the breather amplitude dependence of the distance to the band edge, see Fig. 8.1(c). For small values of Δq (and hence ε) the agreement is very good. The growth parameter gives an indication of how wide or narrow the breather will be, with larger growth parameters corresponding to narrower solutions. The prediction from the linear theory is given by the real part of the Floquet exponent corresponding to mode m_0, and the approximation from the perturbation analysis is (7.11). A comparison of these two quantities are shown as the red markers and lines, respectively of Fig. 8.1(c). The trends in Fig. 8.1(c)

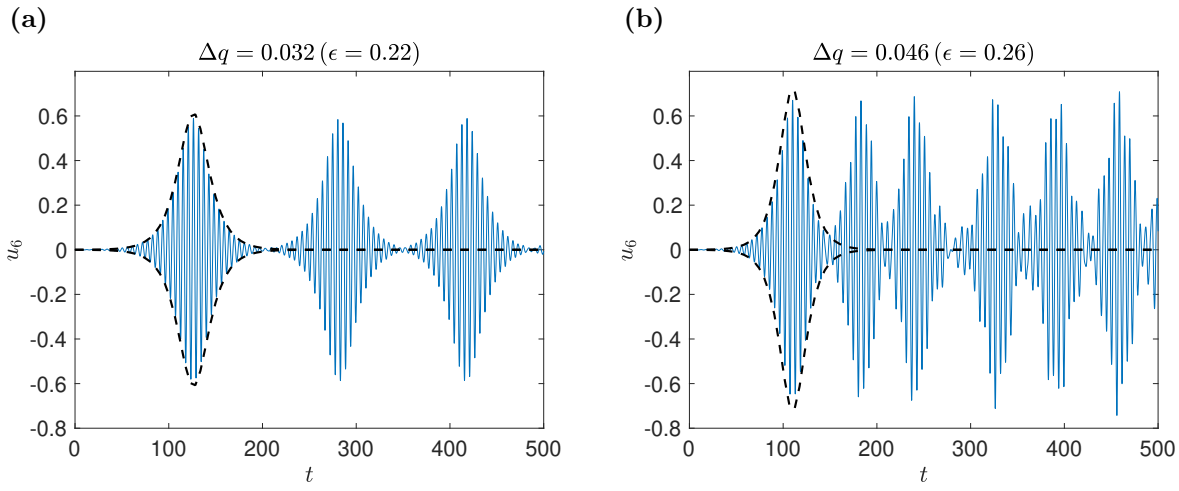

FIG. 8.2. *Numerical simulation with all parameters as in Fig. 8.1 but larger values of ε.* ***(a)*** *With $\Delta q = 0.032$ ($\varepsilon = 0.22$) a temporally localized structure is initially observed, but over a longer time interval a recurrence of breathing patterns emerges. The dashed line shows an approximation of the envelope given by Eq. (8.2).* ***(b)*** *With $\Delta q = 0.046$ ($\varepsilon = 0.26$) the second breather like structure emerges before the temporal localization of the first pulse can be achieved. The envelope approximation given by Eq. (8.2) is still quite good until the breakdown of the temporal localization.*

demonstrate that the q-gap breathers becomes larger in amplitude and more narrow as the wavenumber goes deeper into the gap.

In Fig. 8.1(c) the q-gap breathers are generated up until $\Delta q = 0.042$ (which corresponds to $\varepsilon = 0.25$). For $\Delta q = 0$, the width of the wavenumber bandgap is $q_r - q_\ell \approx 0.28$ (where q_r, q_ℓ are the right and left edges of the bandgap, respectively). Thus, the branch of solutions shown Fig. 8.1(c) extends to roughly 15% of the width of the bandgap. For $\Delta q > 0.042$ we did not observe a coherent temporal localization. Indeed, for all the breathers observed numerically, the localization is obtained for a finite interval of time. For longer time simulations the amplitude of the breather can grow again (leading to a repeated appearance of breathers), see Fig. 8.2(a). Similar observations have been made for k-gap solitons in photonic systems [34]. While Theorem 1.1 guarantees that a temporally localized structures exists over a finite temporal interval, there is no statement about the dynamics beyond this interval. The numerical simulations suggest the tail of the breather can experience repeated growth. We observed as Δq becomes larger, the time between consecutive peaks of the pulses becomes smaller. In other words, the emergence of the "second" breather occurs faster as Δq becomes larger. Thus, for sufficiently large Δq the structure is not temporally localized since the second breather emerges "too soon", see Fig. 8.2(b). This is the reason why we only show $\Delta q \leq 0.042$ in Fig. 8.1(c).

Next, we consider an example where the breathers bifurcate from μ_2. The spectral bands corresponding to $c = 0$, $T = 1/0.37$, $K_2 = \underline{m} = 1$, $k_a^0 = 0.5$ and $k_b^0 = 0.7487$ are shown in Fig. 8.3(a). For these parameter values the mode $m_0 = 4$ lies at the bottom of the second spectral band, namely $\lambda(q_4) = \mu_2$. Notice that the concavity of the second spectral band is opposite of the first band, namely $\lambda_2''(\ell_0) > 0$. Thus, in order to satisfy the **(Coeff)** condition, we require $\chi > 0$. If $K_3 = 0$ this implies that $K_4 > 0$ and the sign parameter is now $\delta = -1$. Thus, for the next numerical simulations, we fix $K_3 = 0$ and $K_4 = 0.8$. The approximation given in Eq. (8.2) is identical in this case, but we replace $\lambda_1''(\ell)$ with $\lambda_2''(\ell)$, and likewise for the underlying Bloch modes (where f_1 should be replaced by f_2, etc.).

Figure 8.3(b) shows an example of the generalized q-gap breather with $\varepsilon = 0.1$, with corresponding envelope prediction given by Eq. (8.2). Qualitatively, the results are similar to the example shown in

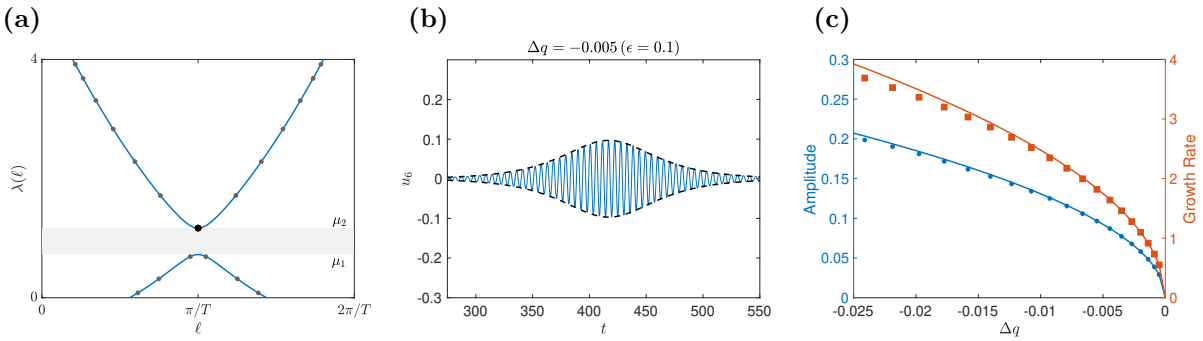

FIG. 8.3. ***(a)*** *Spectral bands (blue curves) of the Schrödinger operator as a function of ℓ, the imaginary part of the Floquet exponent. The gray dots shown the corresponding values in the finite lattice with $N = 10$. The parameter values are $c = 0$, $T = 1/0.37$ and $K_2 = \underline{m} = 1$. The critical modulation amplitude parameters are $k_a^0 = 0.5$ and $k_b^0 = 0.7487$. The critical mode number is $m_0 = 4$, which lies at the bottom of the second spectral band, namely $\lambda(\ell(q_4)) = \mu_2$ (see larger black marker). The eigenvalues μ_1 and μ_2 define the edges of the band gap, shown as the gray shaded region.* ***(b)*** *Example q-gap breather bifurcating from μ_2 with nonlinear coefficients $K_3 = 0$ and $K_4 = 0.8$. The initial value is $u_n(0) = 10^{-4}\sin(q_4 n)$ and $\varepsilon = 0.1$. The displacement of the 6th particle is shown as a function of time. The modulation amplitude is $k_a = k_a^0 + \varepsilon^2 = 0.06$, $k_b = k_b^0 + \varepsilon^2 = 0.7587$. The dashed line shows an approximation of the envelope given by Eq. (8.2) with $\chi = 1.7707$, $\lambda''(\ell_0) = 26.3821$ and $\varepsilon = 0.1$. For this value of ε, the distance of the wavenumber to the edge of the gap is $\Delta q = q_4 - q_r = -0.005$.* ***(c)*** *Plot of the amplitude of the breather ($\max_t u_6(t)$) for the numerical simulation (blue dots) and prediction based on Eq. (8.2) (blue line) as a function of Δq. The real part of the Floquet exponent corresponding to q_4 (solid red squares) and asymptotic approximation $\varepsilon\sqrt{\delta\lambda''(\ell_0)/2}$ (red line) are also shown, which indicate the growth (decay) rate of the q-gap breather.*

Fig. 8.1(a). Figure 8.3(c) shows the dependence of the breather amplitude and growth rate on the parameter $\Delta q = q_r - q_{m_0}$. Note, since the breather is bifurcating from the right edge of the wavenumber bandgap, the quantity Δq will be negative. The breather amplitude grows like $\mathcal{O}(\sqrt{|\Delta q|})$.

8.2. Examples with $c = 0$ and $K_3 \neq 0$. Here we will consider $K_3 \neq 0$. In particular, we will chose values of the nonlinear coefficients in (1.4) that correspond to the modulated magnetic lattice described in Sec. 1.1 so that the results obtained here are directly relevant for the experimental set-up described in [7]. In the re-scaled variables the interaction coefficients are $K_2 = K_3 = 1$ and $K_4 = 0.8$. Since $K_3 \neq 0$ the sign of χ must be computed directly to see if the relevant eigenvalue to bifurcate from is μ_1 or μ_2. χ will depend on the function $h_2(t)$, which we can obtain by solving Eq. (7.16). It will be convenient to estimate $h_2(t)$ numerically under the constraint that $h_2(t)$ is T periodic, which we achieve using a shooting method. In particular, we apply Newton iterations on the map $F(h^0) = h_2(0; h^0) - h_2(T; h^0)$ where $h_2(t; h^0)$ is the solution of Eq. (7.16) with initial condition $h^0 = (h_2(0), \dot{h}_2(0))^T$. The Jacobian of the map F is simply $I - V(T)$, where I is the 2x2 identity matrix and $V(T)$ is the solution to the variational equation $\dot{V} = \frac{df}{dh}V$ with initial value $V(0) = I$ where $\frac{df}{dh}$ is the Jacobian corresponding to Eq. (7.16) [20].

In this example, we consider the spectral situation as shown in Fig. 8.3(a), such that $m_0 = 4$ is the critical mode bifurcating from μ_2. In this case, $\lambda''(\ell_0) > 0$, so we chose $\delta = -1$ and we must have $\chi > 0$ to satisfy (**Coeff**). Upon computing $h_2(t)$ with the shooting method and substituting into Eq. (7.20) with $K_3 = 1$ and $K_4 = 0.8$ we find $\chi = 1.997 > 0$, as desired.

Figure 8.4(a) shows a numerical simulation of the lattice with initial displacement $u_n(0) = 10^{-4}\sin(q_4 n)$ and $\varepsilon = 0.1$, and panel (b) shows a simulation with $\varepsilon = 0.22$. By comparing panels (a) and (b), we see once again that the q-gap breather becomes more narrow and larger in amplitude as Δq (and thus ε) increases in magnitude. What is also apparent, especially in panel (b), is that the numerical simulation is asymmetric, namely, the maximum is not simply the minimum reflected about the $u = 0$ line. Evidently, the asymmetric

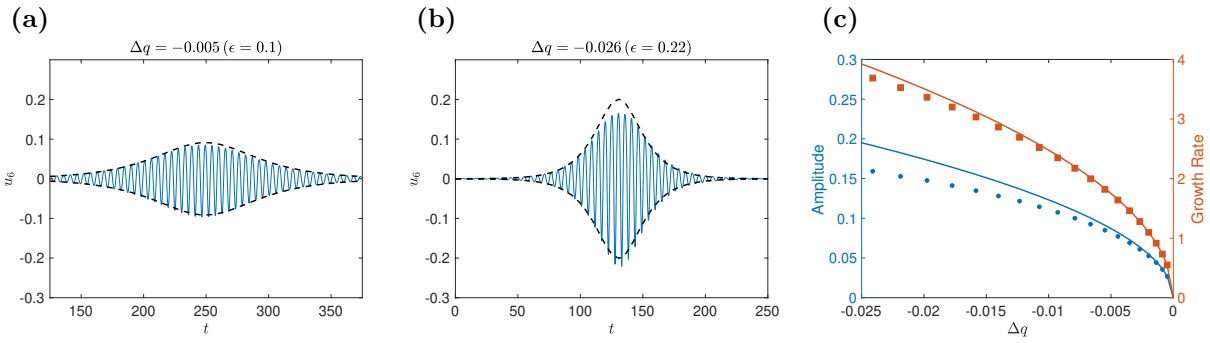

FIG. 8.4. ***(a)*** *A generalized q-gap breather bifurcating from μ_2 with nonlinear coefficients corresponding to a magnetic lattice, namely $K_3 = 1$ and $K_4 = 0.8$. The other parameter values and spectral picture is identical to Fig. 8.3(a). The initial value is $u_n(0) = 10^{-4}\sin(q_4 n)$ and $\varepsilon = 0.1$. The displacement of the 6th particle is shown as a function of time. The modulation amplitude is $k_a = k_a^0 + \varepsilon^2 = 0.06$, $k_b = k_b^0 + \varepsilon^2 = 0.7587$. The dashed line shows an approximation of the envelope given by Eq. (8.2) with $\chi = 1.997$, $\lambda''(\ell_0) = 26.3821$ and $\varepsilon = 0.1$. For this value of ε, the distance of the wavenumber to the edge of the gap is $\Delta q = q_4 - q_r = -0.005$.* ***(b)*** *Same as panel (a) with $\varepsilon = 0.22$.* ***(c)*** *Plot of the amplitude of the breather ($\max_t u_6(t)$) for the numerical simulation (blue dots) and prediction based on Eq. (8.2) (blue line) as a function of Δq. The real part of the Floquet exponent corresponding to q_4 (solid red squares) and asymptotic approximation (7.11) (red line) are also shown, which indicate the growth (decay) rate of the breather.*

nature of the FPUT potential with $K_3 \neq 0$ is manifested through a lack of reflection symmetry in the q-gap breather profile. Asymmetric breathing profiles are well known in space-periodic FPUT systems with quadratic nonlinearities [21]. The approximation given by Eq. (8.2) remains symmetric, however, and thus one would expect the approximation not to do as well as in the $K_3 = 0$ case. Indeed, inspection of Fig. 8.3(c) confirms this, where the difference in amplitude between simulation and theory is larger than in the $K_3 = 0$ case (see e.g., Fig. 8.3(c)). Nonetheless, the asymptotic behavior as $\Delta q \to 0$ is correct, and in particular the breather amplitude grows like $\mathcal{O}(\sqrt{|\Delta q|})$.

8.3. Examples with $c \neq 0$ and $K_3 \neq 0$. In our final example, we include the effect of damping and select $\tilde{c} = 0.1$. By definition, $c = \varepsilon\tilde{c}$, so the critical parameter set (when $\varepsilon = 0$) will have $c = 0$, like before. Thus, we consider once again the parameter set that corresponds to Fig. 8.4(a). However, the numerical solutions and asymptotic approximations will have non-zero damping affect for $\varepsilon > 0$. Since the bifurcation scenario is the same as in Fig. 8.4(a) the initial condition for simulations will be of the same form, namely $u_n(0) = 10^{-4}\sin(q_4 n)$. An example lattice simulation with $\varepsilon = 0.1$ is shown in Fig. 8.5(a) where the underlying damping constant is $c = \varepsilon\tilde{c} = 0.01$. The solution experiences an initial growth, with growth rate given by the real part of the $m_0 = 4$ Floquet exponent, but rather then decaying to a near zero amplitude, like in all the previous examples with $c = 0$, the solution approaches steady periodic motion with period $2T$. A longer time evolution of the same solution is shown in Fig. 8.6. In particular, panel (b) shows the dynamics are essentially periodic for t sufficiently larger.

In terms of the Poincaré map $F_j = U(2Tj)$, the trivial solution $U(t) = 0$ is clearly a fixed point. The $2T$-periodic solution that is approached in the dynamic simulation is another fixed point. Thus, the solution shown in Fig. 8.5(a) is a transition front, since it connects two different fixed points.

Another example of the transition front for a larger value of ε is shown in Fig. 8.5(b). Despite the fact that the structure is not temporally localized, the initial dynamics still resemble the "left" side of the q-gap breather. Indeed, the homoclinic approximation from Eq. (8.2) is quite close to the initial front dynamics (see the solid gray line of Fig. 8.5(a)). For this reason, it is still reasonable to measure the amplitude of the front in the same way we measured the amplitude for the q-gap breathers. A plot of the front amplitude and real part of the $m_0 = 4$ Floquet exponent is shown in 8.5(c). The amplitude trend is similar

to the non-damped case, but the magnitude of the amplitude is smaller, as expected (compare panel (c) of Figs. 8.4 and 8.5).

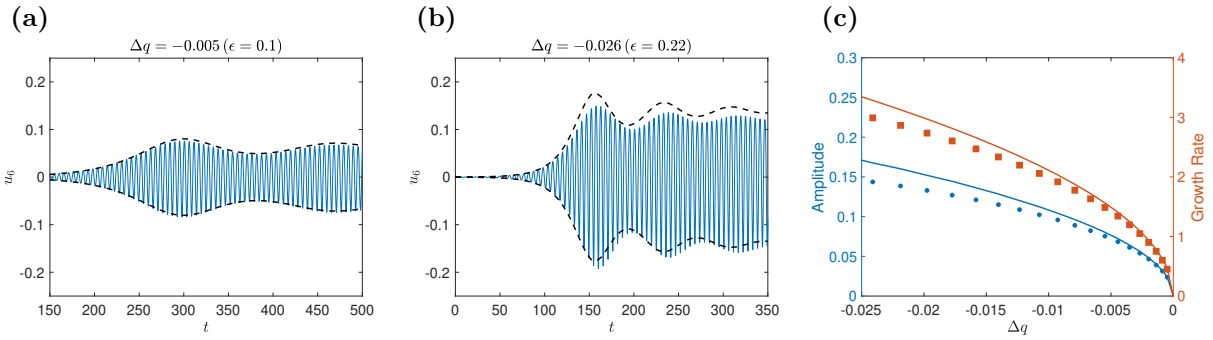

FIG. 8.5. ***(a)*** *A transition front bifurcating from μ_2 with nonlinear coefficients corresponding to a damped magnetic lattice, namely $K_3 = 1$, $K_4 = 0.8$ and $\tilde{c} = 0.1$. The other parameter values and spectral picture is identical to Fig. 8.3(a). The initial value is $u_n(0) = 10^{-4}\sin(q_4 n)$ and $\varepsilon = 0.1$. The displacement of the 6th particle is shown as a function of time. The modulation amplitude is $k_a = k_a^0 + \varepsilon^2 = 0.06$, $k_b = k_b^0 + \varepsilon^2 = 0.7587$ and the damping constant is $c = \varepsilon\tilde{c} = 0.01$. The dashed line shows an approximation of the envelope given by Eq. (7.12) with $\chi = 1.997$, $\lambda''(\ell_0) = 26.3821$ and $\varepsilon = 0.1$. For this value of ε, the distance of the wavenumber to the edge of the gap is $\Delta q = q_4 - q_r = -0.005$.* ***(b)*** *Same as panel (a) with $\varepsilon = 0.22$.* ***(c)*** *Plot of the amplitude of the front ($\max_t u_6(t)$) for the numerical simulation (blue dots) and prediction based on Eq. (7.12) (blue line) as a function of Δq. The real part of the Floquet exponent corresponding to q_4 (solid red squares) and asymptotic approximation $r_0^+\varepsilon$ (red line) are also shown, which indicates the initial growth rate.*

The amplitude equation Eq. (7.18) can be used to approximate the front dynamics. However, the equation does not yield an explicit solution in the presence of damping and so we will employ a qualitative and numerical analysis of Eq. (7.18). A straightforward phase plane analysis shows that the trivial fixed point $(A, A') = (0, 0)$ is a saddle with corresponding eigenvalues $r_0^{\pm} = (-s_3 \pm \sqrt{s_3^2 + 4s_1})/2$ and the fixed points $(A, A') = (\pm\sqrt{s_1/s_2}, 0)$ are spiral-sinks with corresponding eigenvalues $r_1^{\pm} = (-s_3 \pm i\sqrt{8s_1 - s_3^2})/2$ where the s_j are the coefficients of Eq. (7.18), namely,

$$s_1 = \left(\frac{\tilde{c}^2}{4\underline{m}} - \delta\right)\frac{2}{\lambda''(\ell_0)} + \frac{\tilde{c}^2}{4\underline{m}^2} > 0, \qquad s_2 = \frac{2\chi}{\lambda''(\ell_0)} > 0, \qquad s_3 = \frac{\tilde{c}}{\underline{m}} > 0.$$

In the phase plane, there is a heteroclinic orbit that leaves the trivial fixed point along the unstable eigenvector $(1, r_+^0)^T$ and approaches the $(\sqrt{s_1/s_2}, 0)$ fixed point. There is another heteroclinic orbit that leaves the trivial fixed point along the unstable eigenvector $(-1, -r_+^0)^T$ and approaches the $(-\sqrt{s_1/s_2}, 0)$ fixed point, see Fig. 6.1. To approximate the heteroclinic orbit, we numerically solve Eq. (7.18) with initial condition $A(0) = 10^{-4}$, $A'(0) = 10^{-4}\, r_+^0$. The resulting solution $A(\tau)$ is then used in Eq. (7.12) to generate the approximation of the lattice dynamics.

Examples are shown in Fig. 8.5(a,b), where the envelopes are shown for $\varepsilon = 0.1$ and $\varepsilon = 0.22$, respectively. Once again, the envelope dynamics are captured well by Eq. (7.12), especially for small ε. The periodic oscillation of the envelope can be approximated by the imaginary part of the eigenvalue associated to the non-trivial fixed point, namely $\tau_{\text{env}} = 2\pi/(\sqrt{8s_1 - s_3^2}/2)$. In terms of the original lattice variables this translates to $\tau_{\text{env}}/\varepsilon$. For the example shown in Fig. 8.6(a) with $\varepsilon = 0.1$, the average peak-to-peak time of the envelope is 165.3 time units, where as $\tau_{\text{env}}/\varepsilon = 159.3$, which is quite close.

The front amplitude as a function of Δq is shown as the solid blue line in panel (c), and an approximation of the initial growth rate $r_+^0\varepsilon$ is shown as the red line. Once again the asymptotic behavior as $\Delta q \to 0$ is correct. Despite the presence of damping, the front amplitude grows like $\mathcal{O}(\sqrt{|\Delta q|})$.

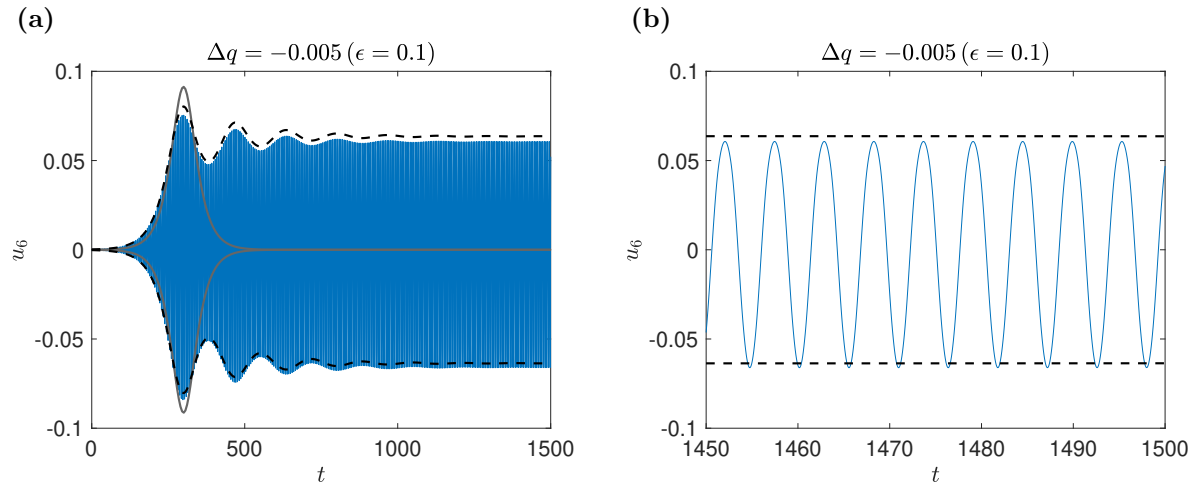

FIG. 8.6. ***(a)*** *Same as Fig. 8.5(a) but over a longer time interval. The dashed line shows an approximation of the envelope given by Eq. (7.12), which accounts for damping. The solid gray line shows the homoclinic approximation (i.e., with no damping) of the envelope given by Eq. (8.2).* ***(b)*** *A zoom of panel (a) for large values of t. Here it can be seen the dynamics are very close to periodic.*

9. Conclusions. Generalized q-gap breathers are coherent structures that are localized in time, periodic in space, and have wavenumber in a q-gap. They are the natural counterpart of the discrete breathers of spatially periodic lattices, which themselves are of fundamental importance in a diverse range of fields.

In the absence of damping, we proved rigorously the existence of generalized q-gap breathers in a time-periodic FPUT lattice using normal form theory. In particular, we proved the existence of oscillating homoclinic solutions over a finite time interval with tails that can be made arbitrarily small, but finite. These solutions bifurcate from one edge of the q-gap. Which of the edges is determined by the nonlinear coefficients K_3, K_4 and the concavity of the spectral band from which the solution bifurcates. The amplitude of the q-gap breather grows like $\mathcal{O}(\sqrt{\Delta q})$, where Δq is the distance of the underlying wavenumber to the band edge. This result makes rigorous the numerical and experimental observations of such q-gap breathers in [7]. We also provided a tractable analytical approximation of such solutions using a multiple-scale analysis and corroborated results with direct numerical simulations.

In the presence of damping we proved the existence of solutions that connect the zero state to a time-periodic one, which we called the transition fronts. The multiple-scale analysis also provided an accurate description of the front solutions, although the underlying amplitude equation needed to be solved numerically. The initial stage of the front dynamics were well described by the undamped q-gap breather approximations.

Generalized q-gap breathers and transition fronts represent new types of nonlinear wave structures. This work provided the first rigorous results in their study, complementing earlier experimental and numerical work. Nonetheless, there are still many open questions regarding q-gap breathers and transition fronts. This includes the possible existence of genuine q-gap breathers (i.e., with both tails decaying to zero), the numerically exact computation of q-gap breathers (i.e., numerical roots of the appropriate map up to a user-prescribed tolerance) and the exploration of such structures in higher spatial dimensions or in settings beyond the FPUT realm. Indeed, any system that is already described by a nonlinear wave equation that could be adapted to be time-varying (in order to induce a q-gap) would be a candidate for the implementation of q-gap breathers. This suggests that q-gap breathers' relevance, and hence the results of this work, could extend to a wide range of fields.

REFERENCES

[1] N. Akhmediev, A. Ankiewicz, and J. M. Soto-Crespo, *Rogue waves and rational solutions of the nonlinear Schrödinger equation*, Phys. Rev. E, 80 (2009), p. 026601.

[2] A. Ankiewicz, N. Akhmediev, and J. M. Soto-Crespo, *Discrete rogue waves of the Ablowitz-Ladik and Hirota equations*, Phys. Rev. E, 82 (2010), p. 026602.

[3] G. P. Berman and F. M. Izrailev, *The fermi-pasta-ulam problem: Fifty years of progress*, Chaos, 15 (2005).

[4] M. Butt, S. Khonina, and N. Kazanskiy, *Recent advances in photonic crystal optical devices: A review*, Optics and Laser Technology, 142 (2021), p. 107265.

[5] L. S. Cao, D. X. Qi, R. W. Peng, M. Wang, and P. Schmelcher, *Phononic frequency combs through nonlinear resonances*, Phys. Rev. Lett., 112 (2014), p. 075505.

[6] M. Centurion, M. A. Porter, Y. Pu, P. G. Kevrekidis, D. J. Frantzeskakis, and D. Psaltis, *Modulational instability in nonlinearity-managed optical media*, Phys. Rev. A, 75 (2007), p. 063804.

[7] C. Chong, B. Kim, E. Wallace, and C. Daraio, *Modulation instability and wavenumber bandgap breathers in a time layered phononic lattice*, Phys. Rev. Research, 6 (2024), p. 023045.

[8] T. Dauxois, *Fermi, Pasta, Ulam, and a mysterious lady*, Phys. Today, 61(1) (2008), p. 55.

[9] S. V. Dmitriev, E. A. Korznikova, Y. A. Baimova, and M. G. Velarde, *Discrete breathers in crystals*, Physics-Uspekhi, 59 (2016), pp. 446–461.

[10] T. Dohnal, D. E. Pelinovsky, and G. Schneider, *Travelling modulating pulse solutions with small tails for a nonlinear wave equation in periodic media*, Nonlinearity, 37 (2024), p. 055005.

[11] E. Fermi, J. Pasta, S. Ulam, and M. Tsingou, *Studies of nonlinear problems i*, 1955.

[12] S. Flach and A. Gorbach, *Discrete breathers: advances in theory and applications*, Phys. Rep., 467 (2008), p. 1.

[13] S. Flach, M. V. Ivanchenko, and O. I. Kanakov, *q-Breathers and the Fermi-Pasta-Ulam Problem*, Phys. Rev. Lett., 95 (2005), p. 064102.

[14] R. Fukuizumi and G. Schneider, *Interchanging space and time in nonlinear optics modeling and dispersion management models*, J. Nonlinear Sci., 32 (2022), pp. 29, 39.

[15] G. Gallavotti, *The Fermi–Pasta–Ulam Problem: A Status Report*, Springer-Verlag, Berlin, Germany, 2008.

[16] A. Ganesan, C. Do, and A. Seshia, *Phononic frequency comb via intrinsic three-wave mixing*, Phys. Rev. Lett., 118 (2017), p. 033903.

[17] M. D. Groves and G. Schneider, *Modulating pulse solutions for quasilinear wave equations*, Journal of Differential Equations, 219 (2005), pp. 221–258.

[18] J. Guckenheimer and P. Holmes, *Nonlinear oscillations, dynamical systems, and bifurcations of vector fields*, vol. 42 of Appl. Math. Sci., Springer, Cham, 1983.

[19] W. Hartmann, *Acoustic Signal Processing*, Springer New York, New York, NY, 2007, pp. 503–530.

[20] M. Hirsch, S. Smale, and R. Devaney, *Differential Equations, Dynamical Systems, and an Introduction to Chaos*, Pure and Applied Mathematics - Academic Press, Elsevier Science, 2004.

[21] G. Huang and B. Hu, *Asymmetric gap soliton modes in diatomic lattices with cubic and quartic nonlinearity*, Phys. Rev. B, 57 (1998), p. 5746.

[22] G. Iooss and M. Adelmeyer, *Topics in bifurcation theory and applications.*, vol. 3 of Adv. Ser. Nonlinear Dyn., Singapore: World Scientific, 2nd ed. ed., 1998.

[23] P. G. Kevrekidis, *Non-linear waves in lattices: Past, present, future*, IMA J. Appl. Math., 76 (2011), pp. 389–423.

[24] B. L. Kim, C. Chong, S. Hajarolasvadi, Y. Wang, and C. Daraio, *Dynamics of time-modulated, nonlinear phononic lattices*, Phys. Rev. E, 107 (2023), p. 034211.

[25] B. L. Kim, C. Daraio, C. Chong, S. Hajarolasvadi, and Y. Wang, *Dynamics of time-modulated, nonlinear phononic lattices*, arxiv:, (2022), p. 2209.06511.

[26] I. Kovacic, R. Rand, and S. M. Sah, *Mathieu's equation and its generalizations: Overview of stability charts and their features*, Applied Mechanics Reviews, 70 (2018).

[27] A. B. Kozyrev, H. Kim, and D. W. van der Weide, *Parametric amplification in left-handed transmission line media*, Applied Physics Letters, 88 (2006), p. 264101.

[28] G. Lee, D. Lee, J. Park, Y. Jang, M. Kim, and J. Rho, *Piezoelectric energy harvesting using mechanical metamaterials and phononic crystals*, Commun Phys, 5 (2022), p. 94.

[29] L. Liu, W.-R. Sun, B. A. Malomed, and P. G. Kevrekidis, *Time-localized dark modes generated by zero-wavenumber-gain modulational instability*, Phys. Rev. A, 108 (2023), p. 033504.

[30] E. Lombardi, *Orbits homoclinic to exponentially small periodic orbits for a class of reversible systems. Application to water waves*, Arch. Ration. Mech. Anal., 137 (1997), pp. 227–304.

[31] J. Marconi, E. Riva, M. Di Ronco, G. Cazzulani, F. Braghin, and M. Ruzzene, *Experimental Observation of Nonreciprocal Band Gaps in a Space-Time-Modulated Beam Using a Shunted Piezoelectric Array*, Physical Review Applied, 13 (2020), p. 031001.

[32] S. Mukherjee and M. C. Rechtsman, *Observation of unidirectional solitonlike edge states in nonlinear floquet topological insulators*, Phys. Rev. X, 11 (2021), p. 041057.

[33] H. Nassar, B. Yousefzadeh, R. Fleury, M. Ruzzene, A. Alù, C. Daraio, A. N. Norris, G. Huang, and M. R. Haberman, *Nonreciprocity in acoustic and elastic materials*, Nature Reviews Materials, 5 (2020), p. 667–685.

[34] Y. Pan, M.-I. Cohen, and M. Segev, *Superluminal k-gap solitons in nonlinear photonic time crystals*, Phys. Rev. Lett., 130 (2023), p. 233801.
[35] D. A. Powell, I. V. Shadrivov, and Y. S. Kivshar, *Multistability in nonlinear left-handed transmission lines*, Applied Physics Letters, 92 (2008), p. 264104.
[36] ———, *Asymmetric parametric amplification in nonlinear left-handed transmission lines*, Applied Physics Letters, 94 (2009), p. 084105.
[37] Z. Rapti, G. Theocharis, P. G. Kevrekidis, D. J. Frantzeskakis, and B. A. Malomed, *Modulational instability in bose–einstein condensates under feshbach resonance management*, Physica Scripta, 2004 (2004), p. 27.
[38] J. R. Reyes-Ayona and P. Halevi, *Observation of genuine wave vector (k or β) gap in a dynamic transmission line and temporal photonic crystals*, Applied Physics Letters, 107 (2015), p. 074101.
[39] M. Safaei, H. A. Sodano, and S. R. Anton, *A review of energy harvesting using piezoelectric materials: state-of-the-art a decade later (2008–2018)*, Smart Materials and Structures, 28 (2019), p. 113001.
[40] J. A. Sanders, F. Verhulst, and J. Murdock, *Averaging methods in nonlinear dynamical systems*, vol. 59 of Appl. Math. Sci., New York, NY: Springer, 2nd ed. ed., 2007.
[41] M. Soljačić, M. Ibanescu, S. G. Johnson, Y. Fink, and J. D. Joannopoulos, *Optimal bistable switching in nonlinear photonic crystals*, Physical Review E, 66 (2002), p. 055601.
[42] G. Trainiti, Y. Xia, J. Marconi, G. Cazzulani, A. Erturk, and M. Ruzzene, *Time-Periodic Stiffness Modulation in Elastic Metamaterials for Selective Wave Filtering: Theory and Experiment*, Physical Review Letters, 122 (2019), p. 124301.
[43] A. Vainchtein, *Solitary waves in fpu-type lattices*, Physica D, 434 (2022), p. 133252.
[44] F. Y. Wang, G. X. Li, H. L. Tam, K. W. Cheah, and S. N. Zhu, *Optical bistability and multistability in one-dimensional periodic metal-dielectric photonic crystal*, Applied Physics Letters, 92 (2008), p. 211109.
[45] C.-P. Wen, W. Liu, and J.-W. Wu, *Tunable terahertz optical bistability and multistability in photonic metamaterial multilayers containing nonlinear dielectric slab and graphene sheet*, Applied Physics A, 126 (2020), p. 426.
[46] M. Yu, J. K. Jang, Y. Okawachi, A. G. Griffith, K. Luke, S. A. Miller, X. Ji, M. Lipson, and A. L. Gaeta, *Breather soliton dynamics in microresonators*, Nature Communication, 8 (2017), p. 14569.